The EUMETSAT Network of Satellite Application Facilities

ROM SAF
Radio Occultation Meteorology

# ROM SAF CDOP-2

# Visiting Scientist Report 19:

## Further development of BAROCLIM and implementation in ROPP

**Barbara Scherllin-Pirscher**

Danish Meteorological Institute (DMI)
European Centre for Medium-Range Weather Forecasts (ECMWF)
Institut d'Estudis Espacials de Catalunya (IEEC)
Met Office (METO)

Ref: SAF/ROM/DMI/REP/VS19/001
Version: 1.0
Date: 24 June 2013

## DOCUMENT AUTHOR TABLE

| | *Author(s)* | *Function* | *Date* | *Comment* |
|---|---|---|---|---|
| Prepared by: | Barbara Scherllin-Pirscher | ROM SAF Visiting Scientist | 24/6/2013 | |
| Reviewed by (internal): | Stig Syndergaard | ROM SAF Scientist | May 2013 | |
| Approved by: | Kent B. Lauritsen | ROM SAF Project Manager | 24/6/2013 | |

## DOCUMENT CHANGE RECORD

| *Issue/Revision* | *Date* | *By* | *Description* |
|---|---|---|---|
| Draft 1 | 7/5/2013 | BSP | First draft |
| Draft 2 | 10/6/2013 | BSP | Second draft |
| Draft 3 | 21/6/2013 | BSP | Third draft |
| 1.0 | 24/6/2013 | BSP | Final report |
| | | | |

**VS Authors**
This VS study was carried out by Dr. Barbara Scherllin-Pirscher, Wegener Center, Graz; Email: barbara.pirscher@uni-graz.at

**VS Duration**
The VS study was performed at the home institute during December 2012 to April 2013 and included a three days visit in March 2013 to the Danish Meteorological Institute, Copenhagen, Denmark.

**ROM SAF**
The Radio Occultation Meteorology Satellite Application Facility (ROM SAF) is a decentralised processing center under EUMETSAT which is responsible for operational processing of GRAS radio occultation data from the Metop satellites and radio occultation (RO) data from other missions. The ROM SAF delivers bending angle, refractivity, temperature, pressure, and humidity profiles in near-real time and offline for NWP and climate users. The offline profiles are further processed into climate products consisting of gridded monthly zonal means of bending angle, refractivity, temperature, humidity, and geopotential heights together with error descriptions.

The ROM SAF also maintains the Radio Occultation Processing Package (ROPP) which contains software modules that will aid users wishing to process, quality-control and assimilate radio occultation data from any radio occultation mission into NWP and other models.

The ROM SAF Leading Entity is the Danish Meteorological Institute (DMI), with Cooperating Entities: i) European Centre for Medium-Range Weather Forecasts (ECMWF) in Reading, United Kingdom, ii) Institut D'Estudis Espacials de Catalunya (IEEC) in Barcelona, Spain, and iii) Met Office in Exeter, United Kingdom. To get access to our products or to read more about the ROM SAF please go to: http://www.romsaf.org

**Intellectual Property Rights**

# Contents

# Executive summary

Due to beneficial characteristics of Radio Occultation (RO) data in the Upper Troposphere–Lower Stratosphere (UTLS) region, these data are often used in atmospheric and climate research. Above the middle stratosphere, however, the measured bending angle is small compared to the noise, which strongly limits the measurements' quality. When averaging over a large number of profiles, statistical data noise can be reduced, which enables to use data higher up.

In a first study, Foelsche and Scherllin-Pirscher (2012) calculated mean RO bending angles from the FORMOSAT-3/COSMIC (F3C) satellite constellation and showed that these data are of very high quality at least up to an impact altitude of 60 km. Above that altitude, mean bending angles are increasingly affected by residual data noise, which even yields negative mean bending angles above 80 km. Since Foelsche and Scherllin-Pirscher (2012) only used closed-loop F3C data, their mean bending angle profiles do not reach below approximately 8 km.

In this study, I use their mean RO bending angles and extend them with background information at low (below 10 km) and high altitudes (above 80 km) to generate a Bending Angle Radio Occultation Climatology (BAROCLIM) spectral model. To extend mean RO profiles above the Mesopause, I perform statistical optimization from 60 km to 80 km using a best-fitting Mass Spectrometer and Incoherent Scatter Radar (MSIS) profile extracted at a specific latitude, longitude, and month. To extend mean RO profiles down to the surface, I apply a cosine transition from 10 km to 15 km using another best-fitting MSIS profile. Due to the merge of mean RO bending angles and MSIS below 15 km, the BAROCLIM model does not necessarily reflect a true climatology in the lower and middle troposphere.

The BAROCLIM spectral model is expanded into Chebychev polynomials (128 coefficients) and zonal harmonics (18 coefficients). Its evaluation with European Centre for Medium-Range Weather Forecasts (ECMWF) rather reveals deficiencies in ECMWF than in BAROCLIM in the UTLS. While differences are small (<0.5 %) between approximately 15 km and 35 km, larger differences above 40 km are well known biases in ECMWF analyses.

A first, very promising, application of BAROCLIM for bending angle initialization in RO processing and its validation relative to ECMWF clearly shows the potential of BAROCLIM to be used in RO retrieval algorithms.

# 1 Introduction

Radio Occultation (RO) measurements are performed when a satellite in Low Earth Orbit (LEO) receives a Global Navigation Satellite System (GNSS) signal, e.g., of a Global Positioning System (GPS) satellite, which is bent on the path through the atmosphere. The measured quantity onboard the LEO satellite is the excess phase relative to the vacuum phase. In RO data processing, this excess phase can be retrieved to bending angle, refractivity, density, pressure, temperature, and water vapor.

The application of an Abel transformation (see e.g., Melbourne et al. 1994; Hajj et al. 2002) enables the calculation of refractivity $N$ from bending angle $\alpha$:

$$N(r) = (n(r) - 1) \cdot 10^6 = \left( \exp \left[ \frac{1}{\pi} \int_{a_1}^{\infty} \frac{\alpha(a)}{\sqrt{a^2 - a_1^2}} \mathrm{d}a \right] - 1 \right) \cdot 10^6, \tag{1.1}$$

where $n$ the refractive index, $r$ is the distance from the center of curvature, $a$ the impact parameter[1], and $a_1$ the impact parameter for the ray whose tangent radius is $r_1$, $a_1 = n(r_1)r_1$. Since the upper limit of this integral is infinity, it is necessary to initialize the bending angle profile at high altitudes.

A bad initialization of the Abel integral at high altitudes results in errors in the refractivity and in subsequently derived atmospheric parameters. Thus, this initialization is of major importance in order to obtain atmospheric profiles of high quality. RO retrieval centers use different approaches to initialize the Abel integral. Jet Propulsion Laboratory (JPL), e.g., uses an exponential decaying function, the Danish Meteorological Institute (DMI) and German Research Centre for Geosciences (GFZ) use the Mass Spectrometer and Incoherent Scatter Radar (MSIS) climatological model, University Corporation for Atmospheric Research (UCAR) uses the National Center for Atmospheric Research (NCAR) climatology, and the Wegener Center for Climate and Global Change (WEGC) uses European Centre for Medium-Range Weather Forecasts (ECMWF) data for bending angle initialization (see e.g., Ho et al. 2012; Steiner et al. 2013). Recently, Ao et al. (2012) and Gleisner and Healy (2013) introduced a new method, which inverts mean bending angle profiles rather than individual profiles. However, this method reveals weaknesses if the number of averaged profiles is small.

[1]The impact parameter is defined as the perpendicular distance between the center of local curvature and the ray path from either the GPS satellite or the LEO satellite (see e.g., Kursinski et al. 1997).

Foelsche and Scherllin-Pirscher (2012) developed a bending angle climatology using data from the FORMOSAT-3/COSMIC (F3C) satellite constellation. This Bending Angle Radio Occultation Climatology (BAROCLIM) model can easily be used as background model for bending angle initialization if it were available as a spectral model. Thus, this Radio Occultation Meteorology (ROM) Satellite Application Facility (SAF) Continuous Development and Operations Phase (CDOP)-2 visiting scientist activity focuses on generating a BAROCLIM spectral model. The research work mainly addressed

1. *Upgrade the BAROCLIM model using a (searched and fitted) MSIS profile, which is obtained from the MSIS climatology at a specific latitude, longitude, and month. This will improve the reproducibility of the model and help to generate a spectral BAROCLIM model.*

2. *Investigate and implement a solution for handling missing values in the BAROCLIM model in connection with generating a spectral version.*

3. *Generate the spectral BAROCLIM model using spherical harmonics and Chebychev polynomials.*

In Chapter 2 I give a short description of the data sets used in this study, including information on the calculation of mean RO bending angle profiles provided by Foelsche and Scherllin-Pirscher (2012). In Chapter 3 I give detailed information on the generation of the BAROCLIM spectral model as well as on the reconstruction from Chebychev polynomials and zonal harmonics to bending angles. The BAROCLIM spectral model itself is presented and discussed in Chapter 4, which also includes the comparison of the model to MSIS and ECMWF. Summary and conclusions of the findings are drawn in Chapter 5.

# 2 Data

For this study I use mean bending angle profiles calculated from Foelsche and Scherllin-Pirscher (2012). Foelsche and Scherllin-Pirscher (2012) used F3C excess phase and orbit data provided by UCAR/COSMIC Data Analysis and Archive Center (CDAAC) and applied the WEGC Occultation Processing System Version 5.5 (OPSv55) processing (revision 2871) to calculate individual ionosphere-corrected non-optimized bending angle profiles as a function of impact altitude[1]. Before averaging over many profiles, Foelsche and Scherllin-Pirscher (2012) applied a twofold outlier rejection to exclude profiles, which strongly affect the mean. For this outlier rejection they excluded i) all profiles with bending angles larger than +40 µrad or smaller than −40 µrad within 50 km and 90 km impact altitude and ii) all profiles with bending angles outside of four standard deviations from the mean profiles in the entire impact altitude range from the surface to 120 km. This quality control removed more than 40 % of all bending angle profiles. However, the number of profiles was still sufficient ($>$ 150 000 for all months) to perform reliable statistics.

Using F3C data from August 2006 to July 2011, Foelsche and Scherllin-Pirscher (2012) calculated monthly mean bending angle profiles for 10°-zonal bands. Since they averaged over all profiles of all years (e.g., all Augusts), there are $18 \times 12 = 216$ mean bending angle profiles available (18 latitude bands, 12 months).

Dependent on atmospheric conditions (i.e., summer or winter conditions) as well as on the number of measurements and related data noise, Foelsche and Scherllin-Pirscher (2012) found negative mean bending angles above 80 km to 90 km. To extend the climatology above these altitudes, they combined mean RO bending angles with profiles from the MSIS climatology. However, they fitted MSIS bending angles in two independent steps (first to individual bending angle profiles and then to averaged data), which makes the reproducibility and further development of the BAROCLIM spectral model more difficult. For that reason, I will not use their BAROCLIM model but perform a more straightforward approach to extend bending angles at high altitudes. Since Foelsche and Scherllin-Pirscher (2012) only used F3C closed-loop data, which do not reach below approximately 8 km, I will also extend mean bending angles down to the surface.

[1] Impact altitude $z$ is the impact parameter $a$ with the local radius of curvature $R_c$ and geoid undulation $N_u$ subtracted.

For this purpose, I use profiles from the MSIS climatology modified for RO applications. MSIS is an empirical model of the neutral atmosphere, which provides atmospheric profiles from the surface up to the thermosphere (Hedin 1991). Høeg et al. (1995) prepared this modified MSIS climatology by fixing local apparent solar time (LT = 0 h), the $F_{10.7}$ solar flux ($F_{10.7} = 150 \times 10^{-22}\,\mathrm{W\,m^{-1}\,Hz^{-1}}$), and the $A_\mathrm{p}$-index ($A_\mathrm{p} = 4$) and by smoothing out a discontinuity at 72.5 km. Stig Syndergaard (DMI) expanded MSIS bending angles $\alpha^{\mathrm{MSIS}}$ and MSIS refractivities $N^{\mathrm{MSIS}}$ into Chebychev polynomials with 32 coefficients and spherical harmonics with 8 coefficients. He generated this MSIS spectral model with different temporal resolutions. I use the version which is available for the 15th of every month.

I do not only use MSIS bending angles to extend mean RO bending angles at high and low altitudes but also to validate the BAROCLIM spectral model.

Furthermore, I use co-located profiles extracted from ECMWF analysis fields with a resolution of T42L91 (model top at approximately 80 km) for BAROCLIM validation. Co-location is obtained from the nearest time layer (ECMWF profiles four analysis fields per day) and spatial interpolation to mean event location.

# 3 Generation of the BAROCLIM spectral model

## 3.1 Upgrade of the BAROCLIM model above the stratosphere

Due to negative neutral atmosphere bending angles above 80 km the mean bending angle profiles have to be combined with additional data. I use profiles from the MSIS spectral model (see above) for this purpose. First, I extract MSIS profiles on a $5° \times 10°$ latitude-longitude grid for each month ($36 \times 36 \times 12 = 15\,552$ profiles in total), searching for the best-fitting profile between $h_{\mathrm{top}} = 80\,\mathrm{km}$ and $h_{\mathrm{bot}} = 60\,\mathrm{km}$. The best-fitting profile is found where

$$\Delta\alpha^2 = \sum_{i=h_{\mathrm{bot}}}^{h_{\mathrm{top}}} (\alpha_i^{\mathrm{RO}} - \alpha_i^{\mathrm{MSIS},k})^2 = \min, \qquad k = 1 \ldots 15\,552. \tag{3.1}$$

The best-fitting profile $\alpha^{\mathrm{bf\,MSIS}}$ is then multiplied with a fit factor, which is obtained from a simple linear regression model also applied to the impact altitude range from 60 km to 80 km

$$f_{\mathrm{fit}} = \frac{\mathrm{Cov}(\alpha^{\mathrm{bf\,MSIS}}, \alpha^{\mathrm{RO}})}{\mathrm{Var}(\alpha^{\mathrm{bf\,MSIS}})}. \tag{3.2}$$

Thus, the MSIS profile used to extend mean RO bending angle profiles at high altitudes is

$$\alpha^{\mathrm{best\,MSIS}} = f_{\mathrm{fit}} \alpha^{\mathrm{bf\,MSIS}}. \tag{3.3}$$

Table 3.1 provides detailed information on these MSIS profiles. In general and with very rare exceptions, the best-fitting MSIS profiles for January and July are extracted either from January ±1 month or from July ±1 month near the correct latitude or from the opposite hemisphere. The MSIS profiles, e.g., that fitted best in January at 65°N/S stem from January at 70°N, 170°W and from February at 80°S, 90°E. The MSIS profiles that fitted best in July at 65°N/S stem from February at 80°S, 130°E and from July at 75°S, 130°E. So, the July-profile at 65°N (summer conditions) is extracted from the model 5 months earlier but it also represents high latitude summer conditions.

Table 3.1 moreover shows that all fit factors are very close to one with differences relative to one being smaller than 0.01. An exception occurs at high southern latitudes

**Table 3.1:** Time $t$ (in months), latitude $\varphi$, and longitude $\lambda$ of the best-fitting top MSIS profiles in January and July for different latitude bands.

| | January | | | | July | | | |
|---|---|---|---|---|---|---|---|---|
| Latitude | $t$ | $\varphi$ | $\lambda$ | $f_{\text{fit}}$ | $t$ | $\varphi$ | $\lambda$ | $f_{\text{fit}}$ |
| 85°N | 7 | 65°S | 100°E | 1.00264 | 12 | 50°S | 120°W | 1.00237 |
| 75°N | 1 | 70°N | 130°W | 1.00122 | 1 | 45°S | 110°E | 0.99519 |
| 65°N | 1 | 70°N | 170°W | 1.00523 | 2 | 80°S | 130°E | 1.00033 |
| 55°N | 1 | 60°N | 170°W | 1.00310 | 1 | 35°S | 40°E | 0.99923 |
| 45°N | 1 | 55°N | 150°E | 0.99938 | 5 | 15°S | 50°W | 1.00518 |
| 35°N | 2 | 50°N | 60°E | 1.00083 | 9 | 30°S | 10°W | 1.00327 |
| 25°N | 7 | 35°S | 70°E | 0.99907 | 8 | 30°S | 40°E | 0.99797 |
| 15°N | 7 | 35°S | 40°W | 1.00069 | 7 | 30°S | 10°W | 1.00346 |
| 5°N | 8 | 35°S | 180°W | 0.99594 | 7 | 25°S | 150°E | 0.99414 |
| 5°S | 9 | 70°N | 160°W | 0.99812 | 7 | 30°S | 20°W | 1.00632 |
| 15°S | 7 | 30°S | 170°E | 0.99554 | 7 | 30°S | 10°W | 1.00459 |
| 25°S | 8 | 30°S | 90°E | 0.99679 | 8 | 35°S | 30°E | 0.99824 |
| 35°S | 9 | 30°S | 20°W | 1.00627 | 2 | 50°N | 50°E | 0.99692 |
| 45°S | 5 | 15°S | 40°W | 1.00169 | 1 | 70°N | 130°E | 1.00024 |
| 55°S | 1 | 35°S | 160°E | 0.99969 | 8 | 75°S | 140°E | 0.99946 |
| 65°S | 2 | 80°S | 90°E | 0.99743 | 7 | 75°S | 130°E | 1.00156 |
| 75°S | 11 | 85°S | 60°W | 1.00416 | 6 | 80°S | 140°W | 0.99333 |
| 85°S | 12 | 50°S | 170°E | 0.99762 | 6 | 85°S | 110°E | 0.89722 |

(85°S) in July, where the fit factor only amounts to 0.897 22 and the difference relative to one is an order of magnitude larger (>0.1). This large fit factor difference might come from the very cold polar vortex over Antarctica, which is not represented in the MSIS climatology.

After obtaining these profiles, I again follow Foelsche and Scherllin-Pirscher (2012) and apply statistical optimization by inverse covariance weighting between 60 km and 80 km to combine the mean RO bending angle profile $\alpha^{\text{RO}}$ with the corresponding MSIS profile $\alpha^{\text{best MSIS}}$:

$$\alpha^{\text{opt}} = \alpha^{\text{best MSIS}} + \mathbf{B}(\mathbf{B}+\mathbf{O})^{-1}(\alpha^{\text{RO}} - \alpha^{\text{best MSIS}}), \tag{3.4}$$

with $\alpha^{\text{opt}}$ being the statistically optimized bending angle profile, and $\mathbf{B}$ and $\mathbf{O}$ being the corresponding background error and observation error covariance matrices, respectively.

**B** and **O** are calculated from

$$\mathbf{B}_{ij} = \sigma_i^{\text{best MSIS}} \sigma_j^{\text{best MSIS}} \exp\left(-\frac{|a_i - a_j|}{L^{\text{best MSIS}}}\right), \tag{3.5}$$

$$\mathbf{O}_{ij} = \sigma_i^{\text{RO}} \sigma_j^{\text{RO}} \exp\left(-\frac{|a_i - a_j|}{L^{\text{RO}}}\right), \tag{3.6}$$

with $a_i$ and $a_j$ being impact altitudes at levels $i$ and $j$, $\sigma_i^{\text{best MSIS}}$, $\sigma_j^{\text{best MSIS}}$ and $\sigma_i^{\text{RO}}$, $\sigma_j^{\text{RO}}$ the background and observational errors at these impact altitude levels, and $L^{\text{best MSIS}} = 15\,\text{km}$ and $L^{\text{RO}} = 2\,\text{km}$ the error correlation lengths for the MSIS model and the mean RO profiles, respectively.

To avoid a too sharp transition at the top and the bottom end of statistical optimization, the background error $\sigma^{\text{best MSIS}}$ is assumed to increase linearly from 0 % at 80 km to 15 % at 78 km, remains 15 % between 78 km and 62 km and then increases linearly from 15 % at 62 km to 100 % at 60 km. All these percent-values refer to the absolute values of the MSIS bending angle at the respective impact altitude level. The observational error $\sigma^{\text{RO}}$ is set to the mean background error between 62 km and 78 km and is constant with height.

The ratio of the retrieval error and the a priori error (Retrieval to A priori Error Ratio (RAER)) is a measure of relative importance of MSIS and RO information. It is given by (Rieder and Kirchengast 2001)

$$\text{RAER} = 100 \frac{\sigma^{\text{ret}}}{\sigma^{\text{best MSIS}}} \tag{3.7}$$

where $\sigma^{\text{ret}}$ contains the square root of the diagonal elements of the retrieval error **R**, which is given by

$$\mathbf{R} = (\mathbf{B}^{-1} + \mathbf{O}^{-1})^{-1}. \tag{3.8}$$

The RAER profile is given in percent. Due to the choice of the background error $\sigma^{\text{best MSIS}}$ and the observational error $\sigma^{\text{RO}}$, the statistically optimized bending angle is background-dominated at the higher end of the transition (RAER $> 50\,\%$) and data-dominated at the lower end of the transition (RAER $< 50\,\%$). The impact altitude, where the retrieval to a priori error ratio equals 50 % (zRAER50) denotes the transition impact altitude between background-dominated and data-dominated altitude regions. Using the settings specified above, zRAER50 always amounts to 67.2 km.

Figure 3.1 exemplary shows RO and MSIS bending angle profiles, their differences relative to the statistically optimized profile, and their error estimates for January, 45°N and 45°S. The smooth statistically optimized bending angle indicates that the settings of statistical optimization are appropriate. Outside of the transition region from 60 km

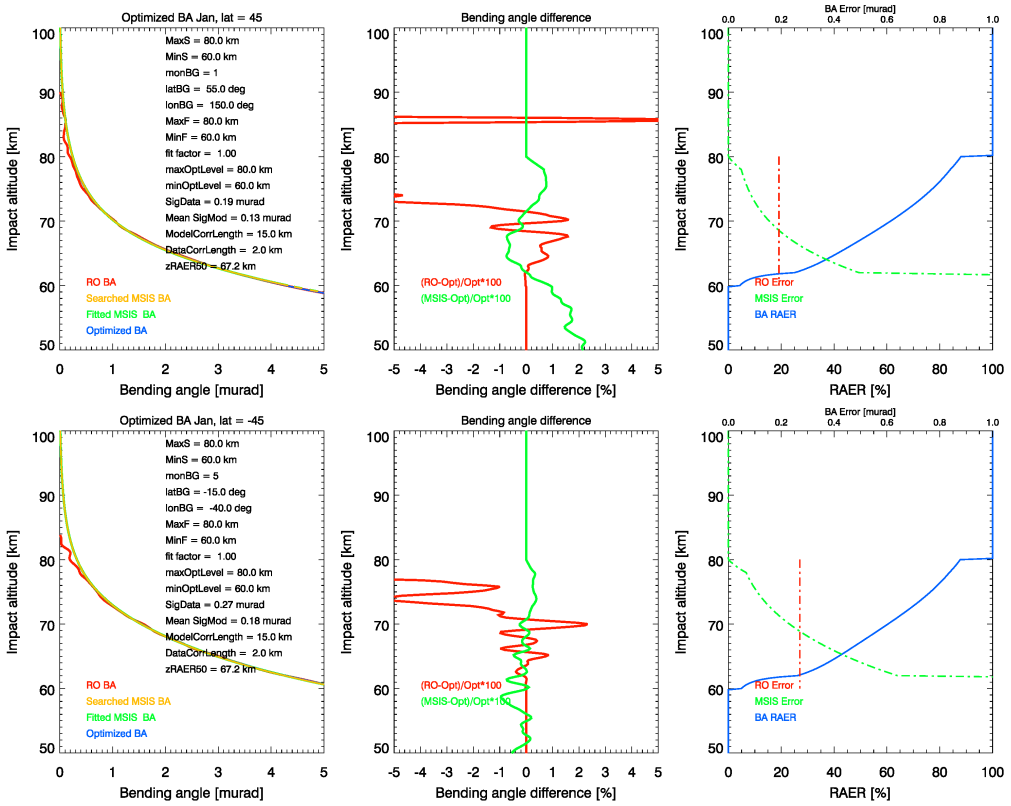


**Figure 3.1:** Mean RO (red), best-fitting MSIS (yellow), fitted MSIS (green), and statistically optimized (blue) bending angle profiles (left), differences between the mean RO/MSIS (red/green) relative to the statistically optimized profile (middle), and RO and background errors (right) in January at 45°N (top) and 45°S (bottom).

to 80 km, the statistically optimized bending angle is equal to MSIS (above 80 km where $\alpha^{\mathrm{opt}} - \alpha^{\mathrm{MSIS}} = 0$) or equal to RO (below 60 km where $\alpha^{\mathrm{opt}} - \alpha^{\mathrm{RO}} = 0$). From 50 km to 80 km differences between MSIS and the statistically optimized bending angle are, in general, within 1 %. Because of small bending angles and comparatively large noise, differences between the mean RO bending angle and the statistically optimized bending angle are larger than 5 % above approximately 72 km. Below 70 km these differences are smaller than 2 %.

## 3.2 Upgrade of the BAROCLIM model in the lower and middle troposphere

Remember that mean RO bending angle profiles calculated from Foelsche and Scherllin-Pirscher (2012) do not reach below approximately 8 km because they did not include F3C open-loop measurements in their calculations but only used F3C closed-loop data. However, to generate a BAROCLIM spectral model it is necessary to extend the climatology down to the surface. For this reason I again extract MSIS profiles on a $5° \times 10°$ latitude-longitude grid for each month (15 552 profiles in total) and search for the best-fitting profile between $h_{\text{top}} = 15$ km and $h_{\text{bot}} = 10$ km applying Eq. (3.1). The fit factor is also estimated between 10 km and 15 km applying Eq. (3.2) for this impact altitude range. The MSIS profiles used to extend the BAROCLIM model down to the surface is then obtained using Eq. (3.3). Instead of applying statistical optimization, I now merge the fitted MSIS profile $\alpha^{\text{best MSIS}}$ and the mean RO profile $\alpha^{\text{RO}}$ using a simple cosine transition from 10 km to 15 km.

Table 3.2 provides detailed information which MSIS profiles are used to extend mean RO bending angle profiles below 10 km. Contrary to the best-fitting MSIS profiles at high altitudes, the best-fitting profiles at low altitudes do not always match months and locations of mean RO profiles. During hemisphere summer, the best-fitting MSIS profile even represents opposite (winter) atmospheric conditions. Better agreement is found in hemispheric winter and at low latitudes. However, similar to best-fitting MSIS profiles at high altitudes, fit factors are again close to one and differences relative to one are smaller than 0.01 everywhere.

Figure 3.2 (left panel) shows that the best-fitting MSIS profile is, in general, close to the mean RO profile above approximately 8 km but differences (middle panels) are distinctively larger below. Furthermore, there is a wiggle in the transition region of almost 1 % in the difference profile between the mean RO and the merged profile. This wiggle does not only occur in these two selected profiles but in all months in almost all latitude regions (not shown). Since the main focus of this study is to provide a BAROCLIM spectral model, which can be used to initialize the Abel integral at high altitudes rather than providing high quality profiles in the lower troposphere, this difference should not cause for concern but it limits the validity of BAROCLIM in the middle troposphere.

## 3.3 Generation of the spectral model

More than 15 years ago, Stig Syndergaard (DMI) expanded MSIS refractivities and bending angles into Chebychev polynomials and spherical harmonics. To generate the BAROCLIM spectral model, I closely collaborated with him taking his advice and using (and

**Table 3.2:** Time $t$ (in months), latitude $\varphi$, and longitude $\lambda$ of the best-fitting bottom MSIS profiles in January and July for different latitude bands.

| | January | | | | July | | | |
|---|---|---|---|---|---|---|---|---|
| Latitude | $t$ | $\varphi$ | $\lambda$ | $f_{\text{fit}}$ | $t$ | $\varphi$ | $\lambda$ | $f_{\text{fit}}$ |
| 85°N | 5 | 70°S | 50°E | 1.00060 | 6 | 55°S | 60°E | 1.00343 |
| 75°N | 6 | 70°S | 40°E | 1.00209 | 1 | 50°N | 70°E | 1.00588 |
| 65°N | 6 | 65°S | 20°E | 1.00396 | 12 | 50°N | 20°E | 1.00697 |
| 55°N | 6 | 60°S | 20°E | 1.00439 | 12 | 45°N | 10°W | 0.99984 |
| 45°N | 1 | 50°N | 70°E | 1.00092 | 10 | 40°N | 60°W | 1.00007 |
| 35°N | 10 | 50°N | 0°E | 0.99926 | 10 | 25°S | 90°E | 0.99991 |
| 25°N | 10 | 35°N | 140°W | 1.00091 | 9 | 30°N | 160°E | 1.00011 |
| 15°N | 9 | 30°N | 180°E | 0.99762 | 8 | 15°S | 110°W | 0.99874 |
| 5°N | 10 | 25°N | 130°E | 0.99813 | 11 | 25°S | 90°E | 0.99917 |
| 5°S | 9 | 30°N | 170°E | 0.99858 | 8 | 15°S | 140°W | 0.99667 |
| 15°S | 9 | 30°N | 170°E | 0.99872 | 10 | 25°N | 120°E | 1.00054 |
| 25°S | 12 | 30°S | 70°E | 0.99885 | 4 | 30°N | 160°W | 1.00029 |
| 35°S | 9 | 35°N | 80°E | 0.99975 | 2 | 40°N | 20°E | 1.00102 |
| 45°S | 3 | 40°N | 30°W | 1.00074 | 12 | 50°N | 50°E | 1.00496 |
| 55°S | 1 | 70°N | 50°E | 1.00084 | 6 | 55°S | 50°E | 1.00206 |
| 65°S | 1 | 70°N | 160°E | 1.00181 | 6 | 65°S | 40°W | 1.00046 |
| 75°S | 1 | 65°N | 180°E | 1.00110 | 1 | 65°N | 70°E | 1.00057 |
| 85°S | 1 | 70°N | 180°E | 0.99958 | 1 | 65°N | 80°E | 0.99964 |

somewhat modifying) his code. This section is largely based on Stig's comments.

Monthly mean BAROCLIM fields, which have a horizontal resolution of 10°-zonal bands (hence they do not vary with longitude), are expanded into Chebychev polynomials and zonal harmonics (rather than spherical harmonics).

### 3.3.1 Expansion into Chebychev polynomials

Generally, a polynomial of degree $k_{\max} - 1$ can be represented as an array of coefficients, $c(k)$ with $k = 1, \ldots, k_{\max}$.

The Chebychev polynomial of degree $k$, $T_k(x)$, is given by (Press et al. 1986)

$$T_k(x) = \cos(k \arccos x). \tag{3.9}$$

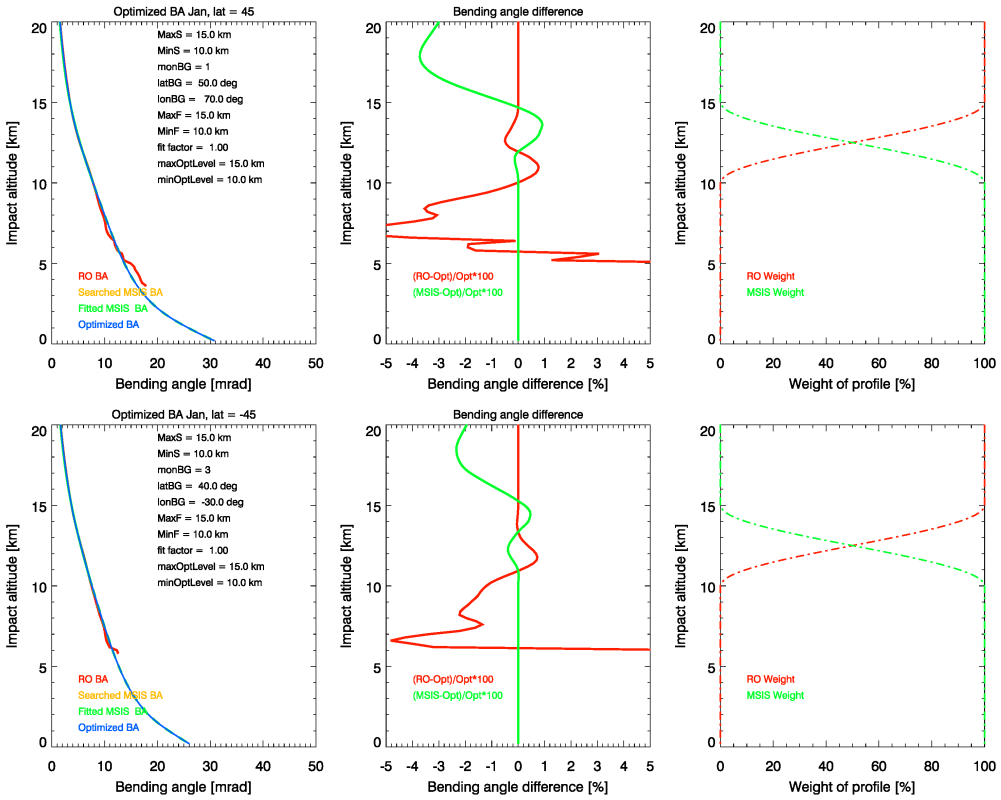


**Figure 3.2:** Mean RO (red), best-fitting MSIS (yellow), fitted MSIS (green), and merged (blue) bending angle profiles (left), differences between the mean RO/MSIS (red/green) and the merged profile (middle), and RO and MSIS weighting functions (right) in January at 45°N (top) and 45°S (bottom).

Explicit expressions for $T_k(x)$ yield (Press et al. 1986)

$$\begin{aligned} T_0 &= 1 \\ T_1 &= x \\ T_2 &= 2x^2 - 1 \\ &\cdots\cdots \\ T_{k+1}(x) &= 2xT_k(x) - T_{k-1}(x) \quad k \geq 1. \end{aligned} \tag{3.10}$$

If Chebychev coefficients $c_j$ are defined by (Press et al. 1986)

$$\begin{aligned} c_j =& \frac{2}{k_{\max}} \sum_{k=1}^{k_{\max}} f(x_k) T_{j-1}(x_k) \\ =& \frac{2}{k_{\max}} \sum_{k=1}^{k_{\max}} f\left[\cos\left(\frac{\pi\left(k-\frac{1}{2}\right)}{k_{\max}}\right)\right] \cos\left(\frac{\pi(j-1)\left(k-\frac{1}{2}\right)}{k_{\max}}\right), \end{aligned} \tag{3.11}$$

where $f(x)$ is an arbitrary function in the interval $[-1, 1]$, $k_{\max}$ is the number of coefficients, and $T_{j-1}(x_k)$ are Chebychev polynomials of degree $(j-1)$ with $j = 1, \ldots, k_{\max}$, the function $f(x)$ can be approximated by

$$f(x) \approx \left[\sum_{k=1}^{k_{\max}} c_k T_{k-1}(x)\right] - \frac{1}{2} c_1. \tag{3.12}$$

Since the function $f(x)$ is limited in the interval $[-1, 1]$ but the BAROCLIM model is available from the surface impact altitude to infinity, it is necessary to change variables.

Following Stig Syndergaard's advice, I do not expand the bending angle itself into Chebychev polynomials but the bending angle scale height $H_S$ (actually the bending angle scale height with a straight line subtracted, see below). The bending angle scale height is more finely structured than the smooth, almost exponentially decreasing bending angle. Figure 3.3 shows the bending angle scale heights as a function of impact altitude for different latitudes calculated from the 10°-zonal mean BAROCLIM field in January and July using

$$H_S(z) = \frac{z}{\ln\left(\alpha_{\text{surf}}/\alpha(z)\right)} \tag{3.13}$$

with $\alpha_{\text{surf}}$ being surface bending angle (for this figure, surface is assumed to be fixed at an impact altitude of 1.7 km at all latitudes), and $\alpha(z)$ being the bending angle at impact altitude $z$.

Above 20 km the scale height approximately amounts to 6.5 km to 7 km with larger scale heights in the summer hemisphere and smaller scale heights in the winter hemisphere. Large seasonal/latitudinal variations are found between 30 km and 80 km with larger variations in July than in January. Below 10 km at high latitudes and 20 km at low latitudes, the scale height strongly decreases and reaches a minimum at the surface. From 100 km to 120 km there are hardly any latitudinal variations and the scale height reaches a constant value of about 6.5 km.

The scale height $H_S$ depends on the surface bending angle $\alpha_{\text{surf}}$ (see Eq. (3.13)), which requires a better knowledge of the surface impact altitude when expanding Chebychev polynomials. The Earth's surface impact altitude is estimated from MSIS refractivity

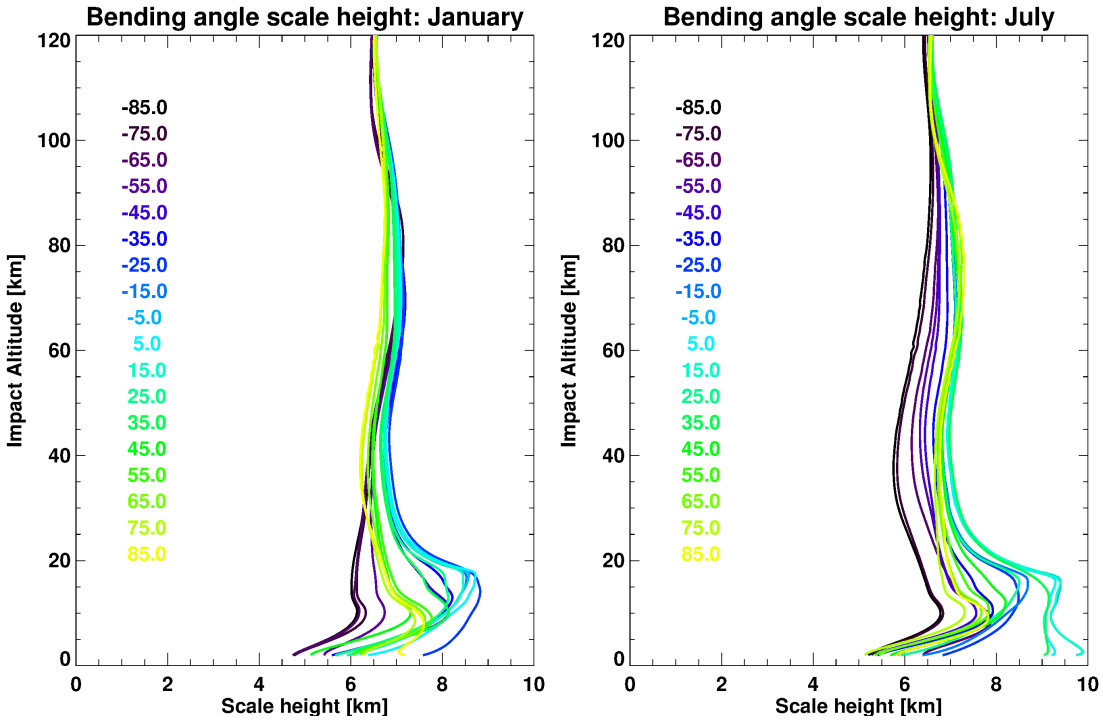


**Figure 3.3:** Bending angle scale height as a function of impact altitude for different latitudes in January (left) and July (right).

$N_{\text{surf}}^{\text{MSIS}}$ at height $h = 0$ (surface), which is extracted for the 15th of the corresponding month, at latitude $\varphi$, and longitude $\lambda = 0$. The surface impact altitude $z_{\text{surf}}$ is then obtained from

$$\begin{aligned} n_{\text{surf}} &= 1 + 10^{-6} N_{\text{surf}}^{\text{MSIS}} \\ a_{\text{surf}} &= R_{\text{Earth}} n_{\text{surf}} \\ z_{\text{surf}} &= a_{\text{surf}} - R_{\text{Earth}} \end{aligned} \tag{3.14}$$

where $n_{\text{surf}}$ is the refraction index at the Earth's surface and $R_{\text{Earth}} = 6371\,\text{km}$ is the mean radius of the Earth. Eq. (3.14) is equivalent to

$$z_{\text{surf}} = R_{\text{Earth}} 10^{-6} N_{\text{surf}}^{\text{MSIS}}. \tag{3.15}$$

The surface impact altitude $z_{\text{surf}}$ depends on atmospheric conditions and varies with latitude and month. It is larger at high latitudes $z_{\text{surf}} \approx 2\,\text{km}$ than at low latitudes

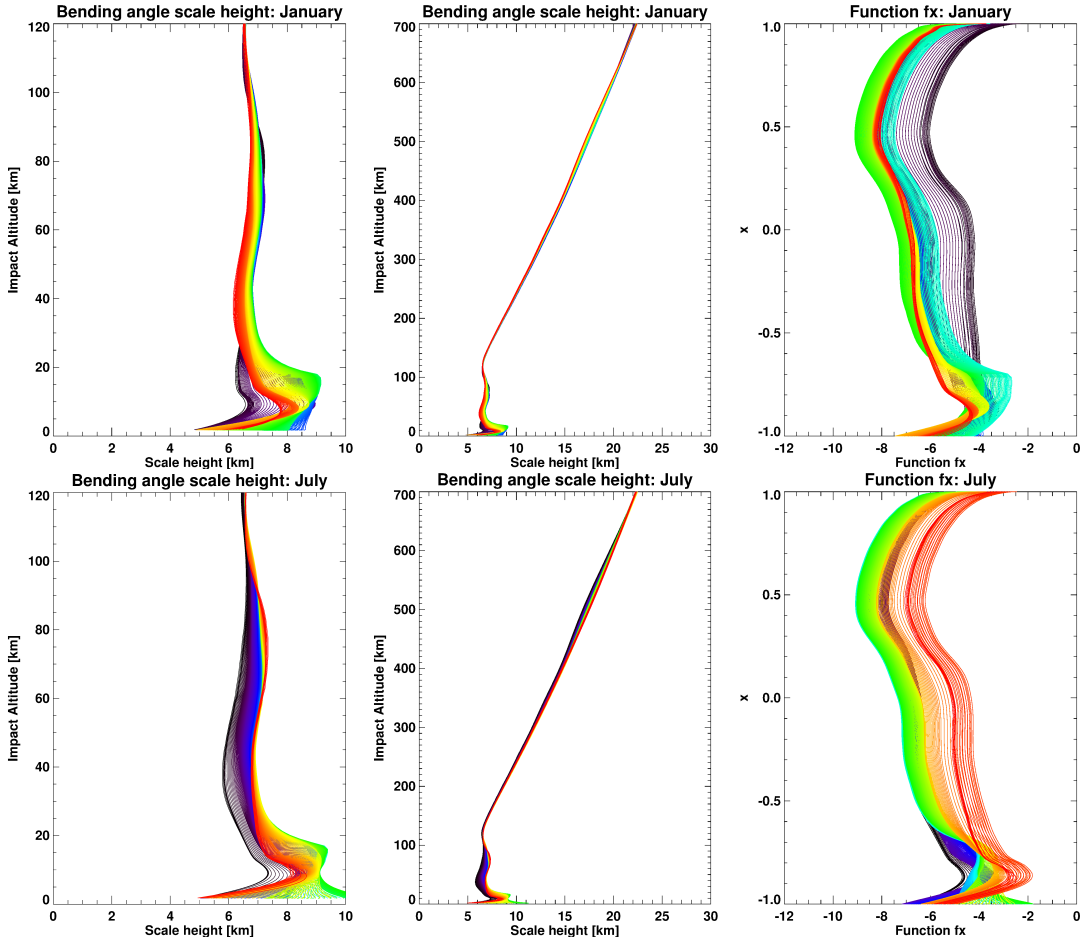


**Figure 3.4:** Bending angle scale heights as a function of impact altitude from the surface to 120 km (left) and to 700 km (middle) and function $f(x)$ put into the Chebychev polynomials (right) for different latitudes (from high southern latitudes (dark blue) via low latitudes (green) to high northern latitudes (red) in January (top) and July (bottom).

$z_{\text{surf}} \approx 1.6$ km. To calculate the bending angle scale height $H_{\text{S}}(z)$, $\alpha_{\text{surf}}$ of the BAROCLIM model is extracted at the surface impact altitude.

Oversampling of each monthly mean BAROCLIM field, bending angle profiles are extracted at 257 grid points from the South Pole ($\varphi = 90°$S) to the North Pole ($\varphi = 90°$N). Since BAROCLIM is a 10°-zonal mean field, the southernmost and northernmost grid points are located at 85°S and 85°N, respectively. To extract bending angles also polewards of 85°S/85°N, I fit a parabola considering bending angles at 75°S/75°N and

85°S/85°N. Bending angles at other latitudes are linearly interpolated from neighboring grid points.

Left panels of Figure 3.4 show the bending angle scale heights obtained from the better surface impact altitude estimate for all 257 latitudes. These bending angle scale heights are in very good agreement with bending angle scale heights shown in Figure 3.3, which confirms that the surface impact altitude of $z_{\mathrm{surf}} = 1.7\,\mathrm{km}$ chosen to plot Figure 3.3 was a reasonable choice. At high altitudes (above approximately 130 km, see middle panels of Figure 3.4) the scale heights approximate a straight line, which can be described by the equation of the line $H_{\mathrm{S}}(z) = mq + b$, with $m$ being the slope, $b$ being the intercept, and $z$ being $q \cdot 100$.

In order to estimate $m$ and $b$, BAROCLIM bending angles are extracted at very high altitudes. After a change of variable from $q$ to $y$ with $q = (1+y)/(1-y)$, the top altitude $z \to \infty$ corresponds to $y = 1$. Four bending angles are extracted at $y = [0.98, 0.96, 0.94, 0.92]$ corresponding to approximately 9900 km, 4900 km, 3233 km, and 2400 km[1] with $z$ being again $100 \cdot q$. This allows for the calculation of bending angle scale heights $H_{\mathrm{S}}(z)$ using again Eq. (3.13). Finally, the function $f_y$ is calculated for each of these four samples from $f_y = H_{\mathrm{S}}(z)/(q+1)$, which approaches $f_y \to (mq+b)/(q+1)$ for $q \to \infty$ ($y \to 1$).

At $y = 1$ the function $f_y$ can be obtained from

$$f_y(1) = 3f_y(0.98) - 3f_y(0.96) + f_y(0.94) \tag{3.16}$$

and its derivative is

$$f'_y(1) = \frac{26}{6} f_y(0.98) - \frac{57}{6} f_y(0.96) + \frac{42}{6} f_y(0.94) - \frac{11}{6} f_y(0.92). \tag{3.17}$$

Finally $m = \lim_{y\to 1}(H_{\mathrm{S}}(z))/(q+1) = f_y(1)$ because $(mq+b)/(q+1) \to m$ for $q \to \infty$ and $b = m - 2f'_y(1)$ because $f'_y(1) = \mathrm{d}/\mathrm{d}y(H_{\mathrm{S}}(z)/(q+1)) \to 1/2(m-b)$. The slope $m$ and the intercept $b$ are further used to calculate Chebychev coefficients.

However, before doing that the bending angle scale height $H_{\mathrm{S}}$ has to be calculated at other impact altitudes. First, the variable $x$ is calculated from

$$x = \cos\left(\frac{\pi\left(k - \frac{1}{2}\right)}{k_{\max}}\right) \tag{3.18}$$

with $k = 1, \ldots, k_{\max}$ and $k_{\max}$ being the number of Chebychev coefficients. $x$ is again defined within the interval $[-1, 1]$. Note that the Chebychev polynomial $T_{k_{\max}}(x)$ has

[1] Note that bending angles are not extracted at these altitudes but at these altitudes with the surface impact altitude added.

$k_{\max}$ zeros in the interval $[-1, 1]$, and they are exactly located at these points $x$ (Press et al. 1986). Impact altitude $z$ is now mapped to $x$ using $q = (\ln 2 - \ln(1 - x))$ and $z = 100 \cdot q$. This mapping function yields a finer vertical spacing at low altitudes and coarser vertical spacing at higher altitudes. The bending angle scale height is again calculated according to Eq. (3.13). The function $f_x$ is obtained from

$$f_x = H_{\mathrm{S}}(z) - (mq + b), \tag{3.19}$$

shown in the right panel of Figure 3.4.

This function is finally used to calculate Chebychev coefficients $c_j$ (see Eq. (3.11)):

$$c_j = \frac{2}{k_{\max}} \sum_{k=1}^{k_{\max}} (H_{\mathrm{S}}(z) - (mq + b)) \cos\left(\frac{\pi(j-1)\left(k - \frac{1}{2}\right)}{k_{\max}}\right). \tag{3.20}$$

Beside the Chebychev coefficients $c_j$, there are also the scalars of the surface impact altitude $z_{\mathrm{surf}}$, surface bending angle $\alpha_{\mathrm{surf}}$, slope $m$, and intercept $b$ of the equation of the line, that need to be held track. All these parameters are expanded into zonal harmonics.

### 3.3.2 Expansion into zonal harmonics

If $f(x)$ is a function defined from $x = -1$ to $x = +1$, it can be written as

$$f(x) = A_0 P_0(x) + A_1 P_1(x) + A_2 P_2(x) + \cdots = \sum_{n=0}^{\infty} A_n P_n(x) \tag{3.21}$$

with $A_n$ being zonal harmonics coefficients

$$A_n = \frac{2n+1}{2} \int_{-1}^{+1} f(x) P_n(x)\, \mathrm{d}x \tag{3.22}$$

and $P_n(x)$ being Legendre Polynomials, which are orthogonal functions on $[-1, 1]$ (see e.g., Spiegel 1979). Equation (3.22) means that each $A_n$ is found by integrating $f(x)P_n(x)$.

The first two Legendre polynomials $P_0(x)$ and $P_1(x)$ are given by

$$P_0(x) = 1 \tag{3.23}$$
$$P_1(x) = x. \tag{3.24}$$

Other Legendre polynomials can be calculated using the recurrence formula (Spiegel 1979)

$$P_{n+1}(x) = \frac{2n+1}{n+1} x P_n(x) - \frac{n}{n+1} P_{n-1}(x), \tag{3.25}$$

which is equivalent to

$$\begin{aligned} P_n(x) =& \frac{2n-1}{n} x P_{n-1}(x) - \frac{n-1}{n} P_{n-2}(x) \\ =& \frac{1}{n}\left[(2n-1)xP_{n-1}(x) - (n-1)P_{n-2}(x)\right] \qquad n \geq 2. \end{aligned} \tag{3.26}$$

As mentioned above, the variable $x$ has to be defined in the interval $[-1, 1]$. In order to determine the zonal harmonics coefficients for $c_j$, $z_{\text{surf}}$, $\alpha_{\text{surf}}$, $m$, and $b$, I use

$$x = \sin\varphi = \cos\vartheta \tag{3.27}$$

with $\varphi$ being geographical latitude, and $\vartheta$ being co-latitude (the complementary angle of the latitude). Thus, $x$ ranges from $-1$ (south pole with $\varphi = -90$, $\vartheta = 180$) to $+1$ (north pole with $\varphi = 90$, $\vartheta = 0$), $\Delta x$ is chosen to be $1/256$, resulting in 257 latitude grid points.

Numerical integration in Eq. (3.22) is performed using the composite Simpsons's rule:

$$\begin{aligned} A_n =& \frac{2n+1}{2} \int_{-1}^{+1} f(x) P_n(x)\, \mathrm{d}x \\ \approx& \frac{2n+1}{2} \frac{\mathrm{d}x}{3} \Big[ g_0(x) + 4g_1(x) + 2g_2(x) + 4g_3(x) + 2g_4(x) + \cdots + 4g_{n-1}(x) + g_n(x) \Big], \end{aligned} \tag{3.28}$$

where the function $g_n(x)$ is equal to $f(x)P_n(x)$, $x$ is the sine of the geographical latitude. The function $f(x)$ represents either $c_j(x)$, $z_{\text{surf}}(x)$, $\alpha_{\text{surf}}(x)$, $m(x)$, or $b(x)$. For each of these parameters, I extract $n_{\max}$ zonal harmonics coefficients. Thus, the final output of the BAROCLIM spectral model are $n_{\max}$ zonal harmonics of these parameters.

### 3.3.3 Reconstruction of BAROCLIM data

The Clenshaw's recurrence formula can be used to efficiently evaluate a sum of coefficients times functions that obey a recurrence formula (Press et al. 1986), e.g.,

$$f(x) = \sum_{l=0}^{l_{\max}} p_l \phi_l(x), \tag{3.29}$$

with $\phi(x)$ satisfying the recurrence relation

$$\phi_{l+1}(x) + \alpha_l(x)\phi_l(x) + \beta_l(x)\phi_{l-1}(x) = 0 \tag{3.30}$$

for some functions $\alpha_l(x)$ and $\beta_l(x)$. To evaluate the linear combination of zonal harmonics and Chebychev polynomials, I apply this method.

First, a function $b_l(x)$ is defined by the following recurrence:

$$b_{l_{\max}+1}(x) = b_{l_{\max}+2}(x) = 0, \tag{3.31}$$

$$b_l(x) = p_l - \alpha_l(x)b_{l+1}(x) - \beta_{l+1}(x)b_{l+2}(x) \quad l = l_{\max}, \ldots, 1. \tag{3.32}$$

The linear combination of $\phi_l(x)$ satisfies

$$\sum_{l=0}^{l_{\max}} p_l\phi_l(x) = b_0(x)\phi_0(x) + b_1(x)[\phi_1(x) + \alpha_0(x)\phi_0(x)]. \tag{3.33}$$

Inserting the expression for $b_0(x)$, this can also be written as

$$f(x) = \sum_{l=0}^{l_{\max}} p_l\phi_l(x) = [p_0 - \beta_1(x)b_2(x)]\phi_0(x) + b_1(x)\phi_1(x). \tag{3.34}$$

Eqs. (3.31), (3.32), and (3.34) are Clenshaw's recurrence formula, which can be used for evaluating the sum given in Eq. (3.29) (Press et al. 1986).

I first start with the reconstruction of the zonal harmonics coefficients. Rewriting Eq. (3.25) to

$$P_{n+1}(x) - \frac{2n+1}{n+1}xP_n(x) + \frac{n}{n+1}P_{n-1}(x) = 0 \tag{3.35}$$

and comparing it to Eq. (3.30) with $l = n$ yields

$$\phi_l(x) = P_n(x). \tag{3.36}$$

This relation can be used to obtain

$$\phi_n(x) = P_n(x), \tag{3.37}$$

$$\phi_0(x) = P_0(x) = 1, \tag{3.38}$$

$$\phi_1(x) = P_1(x) = x = \cos\vartheta, \tag{3.39}$$

$$\alpha_n(x) = -\frac{2n+1}{n+1}x, \tag{3.40}$$

$$\beta_n(x) = \frac{n}{n+1}. \tag{3.41}$$

Comparing Eq. (3.21) with the upper limit of the sum truncated at $n_{\max}$ and Eq. (3.29) yields

$$p_n = A_n, \tag{3.42}$$

which can be utilized to calculate $b_n(x)$ using Eq. (3.32):

$$b_n(x) = A_n + \frac{2n+1}{n+1} x b_{n+1}(x) - \frac{n+1}{n+2} b_{n+2}(x). \tag{3.43}$$

Evaluating $\beta_n(x)$ (see Eq. 3.41) at $n = 1$ yields $\beta_1(x) = 1/2$. Using all these quantities and inserting them in Eq. (3.34) enables the reconstruction of the function $f(x)$ expanded into zonal harmonics

$$f(x) = \sum_{n=0}^{n_{\max}} A_n P_n(x) = A_0 - \frac{1}{2} b_2(x) + x b_1(x). \tag{3.44}$$

In this way, the Chebychev coefficients $c_j$, the surface impact altitude $z_{\text{surf}}$, surface bending angle $\alpha_{\text{surf}}$, slope $m$, and intercept $b$ of the equation of the line (see Subsection 3.3.2) are reconstructed. However, what is still missing is the reconstruction of the bending angle itself.

I again apply Clenshaw's recurrence formula (Eqs. (3.31), (3.32), and (3.34)) to reconstruct the function $f(x)$ given by Eq. (3.12) knowing Chebyshev coefficients $c_j$. According to Eqs. (3.31) and (3.32) I define a function $d_k(x)$ as

$$d_{k_{\max}+1}(x) = d_{k_{\max}+2}(x) = 0, \tag{3.45}$$

$$d_k(x) = p_k - \alpha_k(x) d_{k+1}(x) - \beta_{k+1}(x) d_{k+2}(x) \qquad k = k_{\max}, \ldots, 1. \tag{3.46}$$

Rewriting Eq. (3.10) to

$$T_{k+1}(x) - 2x T_k(x) + T_{k-1}(x) = 0 \tag{3.47}$$

and comparing it to Eq. (3.30) with $l = k$ yields

$$\phi_l(x) = T_k(x). \tag{3.48}$$

This relation can be used to obtain

$$\phi_k(x) = T_k(x), \tag{3.49}$$
$$\phi_0(x) = T_0(x) = 1, \tag{3.50}$$
$$\phi_1(x) = T_1(x) = x, \tag{3.51}$$
$$\alpha_k(x) = -2x, \tag{3.52}$$
$$\beta_k(x) = 1. \tag{3.53}$$

Rewriting Eq. (3.12) to

$$f(x) \approx \left[\sum_{k=1}^{k_{\max}} c_k T_{k-1}(x)\right] - \frac{1}{2}c_1 = \left[\sum_{k=0}^{k_{\max}-1} c_{k+1} T_k(x)\right] - \frac{1}{2}c_1 \tag{3.54}$$

and comparing it to Eq. (3.29) yields

$$p_k = c_{k+1}, \tag{3.55}$$

which can be utilized to calculate $d_k(x)$ using Eq. (3.46)

$$d_k(x) = c_{k+1} + 2x d_{k+1}(x) - d_{k+2}(x). \tag{3.56}$$

Evaluating $\beta_k(x)$ (see Eq. 3.53) at $k = 1$ yields $\beta_1(x) = 1$. Using all these quantities as well as Eq. (3.34) and inserting them in Eq. (3.54) enables the reconstruction of the function $f(x)$ expanded into Chebychev polynomials

$$f(x) \approx \left[\sum_{k=0}^{k_{\max}-1} c_{k+1} T_k(x)\right] - \frac{1}{2}c_1 = x d_1(x) - d_2(x) + \frac{1}{2}c_1. \tag{3.57}$$

All these calculations are performed using the variable $x$ but actually, bending angle is a function of impact altitude $z$. In Subsection 3.3.1, the impact altitude $z$ was mapped to $x$ using the relation $q = (\ln 2 - \ln(1 - x))$ and $z = 100 \cdot q$. Remapping of $x$ to $z$ yields $x = 1 - 2\exp(-q)$ with $q = z/100$. Thus, the bending angle scale height $H_S$ is

$$H_S = f(x) + (mq + b) \tag{3.58}$$

but in order to make sure that the scale height exactly becomes a straight line for very large $q$, it is multiplied with the factor $\exp\left[-\left(\frac{q}{100}\right)^2\right]$ so that the scale height is actually reconstructed from

$$H_S = f(x)\exp\left[-\left(\frac{q}{100}\right)^2\right] + (mq + b). \tag{3.59}$$

Finally the bending angle can be reconstructed using

$$\alpha(z) = \alpha_{\text{surf}}\exp\left[-\frac{z}{H_S(z)}\right]. \tag{3.60}$$

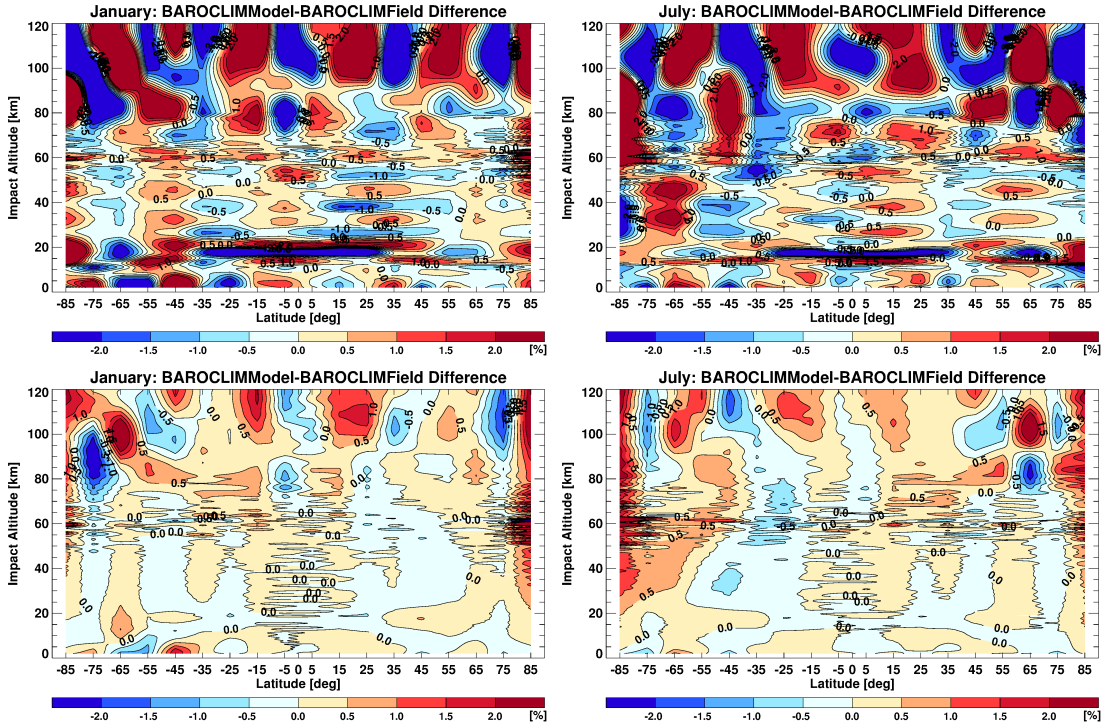


**Figure 3.5:** Systematic difference between the BAROCLIM field and the BAROCLIM spectral model (in %) as a function of latitude and impact altitude for January (left) and July (right). The BAROCLIM spectral model is calculated with 8 zonal harmonics coefficients ($n_{\max} = 7$) and 32 Chebychev coefficients $k_{\max} = 31$ (top) and 22 zonal harmonics coefficients ($n_{\max} = 21$) and 128 Chebychev coefficients ($k_{\max} = 127$) (bottom).

### 3.3.4 Selection of the optimal number of Chebychev coefficients and the degree of zonal harmonics

In order to adjust the order and degree of the Chebychev polynomials and the zonal harmonics, I calculate difference profiles between the BAROCLIM field (10°-zonal bands, 200 m vertical spacing denoted by $\alpha^{\text{field}}$) and the BAROCLIM spectral model $\alpha^{\text{model}}$ for different choices of $k_{\max}$ and $n_{\max}$ aiming at minimizing these differences. Since bending angles decrease exponentially with height, differences are obtained as a percentage difference by

$$\Delta\alpha(z) = \frac{\alpha^{\text{field}}(z) - \alpha^{\text{model}}(z)}{\alpha^{\text{model}}(z)} \cdot 100\,\%. \tag{3.61}$$

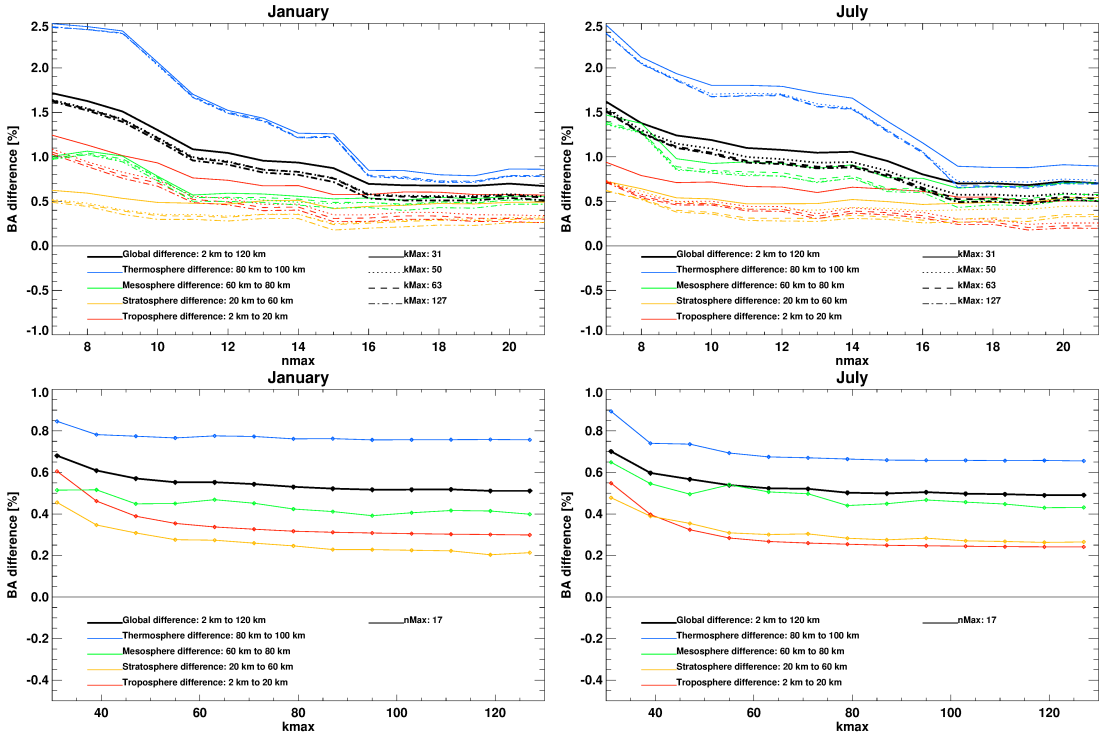


**Figure 3.6:** Absolute amount of differences between the BAROCLIM field and the BAROCLIM spectral model for January (left) and July (right). Top panels show differences as a function of $n_{\max}$ for different $k_{\max}$ (different linestyles) and different altitude layers (different colors). Bottom panels show differences as a function of $k_{\max}$ for different altitude layers (different colors) but with $n_{\max}$ fixed ($n_{\max} = 17$). Please note the different $y$-range of the top and bottom panels.

Figure 3.5 shows differences for two different choices of $n_{\max}$ and $k_{\max}$. Using small $n_{\max}$ and $k_{\max}$ values (top panels of Figure 3.5), the differences between the BAROCLIM field and the BAROCLIM spectral model are larger than $\pm 2\,\%$ above approximately 80 km, below 5 km (mainly in January), and close to the tropical tropopause region. Increasing both, $n_{\max}$ and $k_{\max}$ yields distinctively smaller differences everywhere (see bottom panels of Figure 3.5). However, what is the optimal choice of these two parameters?

In order to determine optimal $n_{\max}$ and $k_{\max}$, I calculate the mean of the absolute amount of the differences for different altitude layers ranging from $z_{\text{bot}}$ to $z_{\text{top}}$ with

impact altitude indices $j_{\text{bot}}$ and $j_{\text{top}}$, respectively,

$$\overline{\Delta\alpha} = \frac{1}{j_{\text{top}} - j_{\text{bot}}} \sum_{j=j_{\text{bot}}}^{j_{\text{top}}} |\Delta\alpha_j| \tag{3.62}$$

and compare results for different choices of $n_{\max}$ and $k_{\max}$.

Top panels of Figure 3.6 show these absolute differences $\overline{\Delta\alpha}$ as a function of $n_{\max}$ for different impact altitude layers and different choices of $k_{\max}$. These figures clearly reveal that differences decrease with increasing $n_{\max}$. A break occurs at $n_{\max} = 16$ (in January) or $n_{\max} = 17$ (in July), which makes sense, because the BAROCLIM field has a horizontal resolution of 10°-zonal bands, which makes 18 zonal bands in total. After obtaining $n_{\max} = 17$ (i.e., 18 zonal harmonics coefficients), I calculate the BAROCLIM spectral model for $k_{\max} = [31, 39, 47, 55, 63, 71, 79, 87, 95, 103, 111, 119, 127]$ and plot the absolute amount of differences for different altitude layers (bottom panels of Figure 3.6).

It is more difficult to determine the best choice of $k_{\max}$ because there is no abrupt break and differences decrease slowly. For this reason, I again plot differences as a function of latitude and impact altitude to see where these differences come from (or rather to see where difference actually decrease with increasing $k_{\max}$), see Figure 3.7.

Even though differences noticeable decrease with increasing $k_{\max}$, they remain larger than 2 % the Mesosphere (above 80 km). This persistent oscillating pattern above 80 km to 100 km might be attributable to the MSIS extrapolation, which does not represent more true latitude variations below. Note that due to the exponential behavior of the bending angle, these relative bending angle differences are still very small in absolute terms. 2 % at 80 km correspond to 0.006 µrad with a bending angle of 0.3 µrad.

In order to set the 0.006 µrad-value in context, I give some information on residual ionospheric errors, which might dominate the BAROCLIM systematic error. Danzer et al. (2013) analyzed day- and night-time Mesospheric bending angles from 65 km to 80 km to estimate the ionospheric residual error and found these differences from 2006 to 2011 (low solar activity) are smaller than 0.05 µrad to 0.1 µrad. Even though these residual ionospheric errors are estimated in a different altitude range it is clear, that 0.006 µrad at 80 km are very small and therefore negligible.

Let us go back to Figure 3.7. Larger, rough bending angle differences are found in the impact altitude range from approximately 55 km to 65 km. Remember, that the bottom end of statistical optimization of MSIS and mean RO bending angles is located at 60 km, i.e., below that height BAROCLIM just relies on RO information. These rough bending angle differences might be caused by remaining RO wiggles, which again result from residual data noise of RO measurements at high altitudes. However, the BAROCLIM spectral model somewhat smooths out these wiggles, which is a good thing.

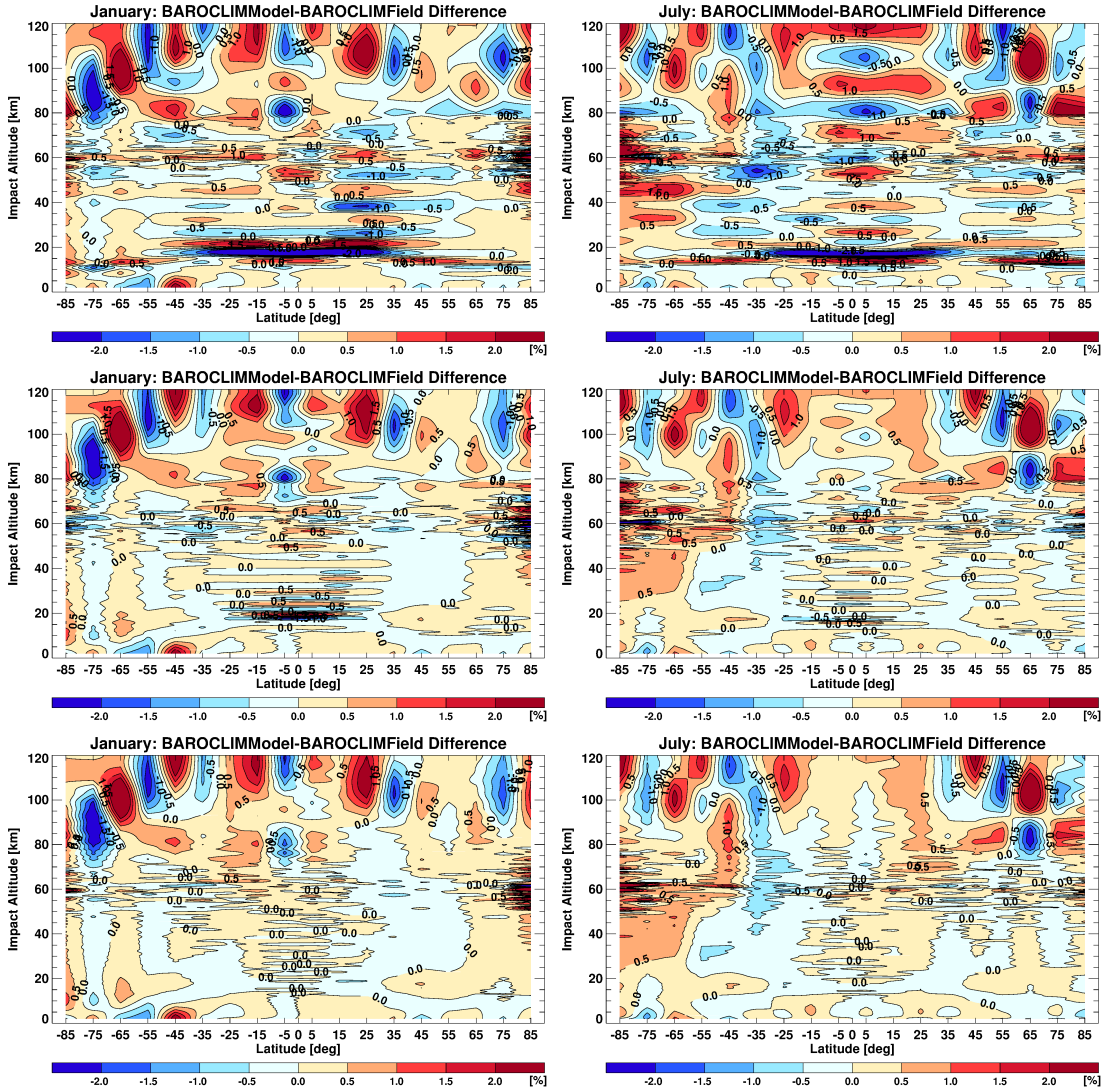


**Figure 3.7:** Systematic difference between the BAROCLIM field and the BAROCLIM spectral model (in %) as a function of latitude and impact altitude for January (left) and July (right). The BAROCLIM spectral model is calculated with 18 zonal harmonics coefficients ($n_{\max} = 17$) and 32 ($k_{\max} = 31$), 64 ($k_{\max} = 63$), and 128 ($k_{\max} = 127$) Chebychev coefficients (top to bottom).

Figure 3.7 also reveals that the differences in the tropical tropopause region decrease

significantly with increasing $k_{\max}$. If the BAROCLIM spectral model should be able to reproduce bending angles close to the tropical tropopause, the number of Chebychev coefficients has to be (at least) equal to 64 but better results are obtained with 128 Chebychev coefficients. Besides the tropical tropopause region, differences for 64 and 128 Chebychev coefficients are very similar.

To better fit the sharp tropical tropopause, I decide to use 128 Chebychev coefficients to generate the BAROCLIM spectral model. However, it is possible to use a smaller $k_{\max}$ when reconstructing the bending angle.

# 4 BAROCLIM model and its validation

## 4.1 The BAROCLIM model

Atmospheric refractivity (hence also bending angle) primarily depend on temperature, pressure, and water vapor. This relationship is given by (Smith and Weintraub 1953; Kursinski et al. 1997)

$$N = 77.6\frac{p}{T} + 3.73 \times 10^5 \frac{e}{T^2} - 4.03 \times 10^7 \frac{n_\mathrm{e}}{f^2} + 1.4W, \tag{4.1}$$

where $p$ is the atmospheric pressure (in hPa), $T$ atmospheric temperature (in K), $e$ partial pressure of water vapor (in hPa), $n_\mathrm{e}$ is the electron density (in electrons $\mathrm{m}^{-3}$), $f$ the transmitter frequency (in Hz), and $W$ is the mass of condensed water in the atmosphere (in $\mathrm{g\,m}^{-3}$).

The first term in Eq. (4.1) represents the contribution of the dry atmosphere, the second term represents the contribution of the moist atmosphere. The ionospheric contribution to refractivity (third term) is very small and only contains ionospheric residuals (see above) if ionospheric correction has already been performed. The last term, which represents the scattering term, is negligible because the content of liquid water is very small compared to the other terms.

From the mid-troposphere upwards the refractivity/bending angle primarily depend on temperature and pressure. In the lower troposphere, especially at low latitudes, water vapor makes a significant contribution to refractivity/bending angle.

In general, neutral atmospheric bending angles as shown in Figure 4.1 are positive, which indicates bending towards the Earth's surface. Furthermore, Figure 4.1 clearly reflects the dependence of the bending angle on different atmospheric parameters. Colder temperatures in the winter hemisphere at high latitudes yield smaller bending angles. This feature is strongest pronounced in the altitude range from approximately 30 km to 90 km. Below 30 km and above 90 km the contour lines do not vary significantly with latitude.

An interesting feature is found in the tropical upper troposphere where 10 000 µrad (i.e., 0.01 rad) and the 3000 µrad (i.e., 0.003 rad) contour lines somewhat diverge. Using a finer bending angle spacing, Ringer and Healy (2008) show that this characteristics is connected to the 0.01 rad isoline, which shows a different latitudinal characteristics than

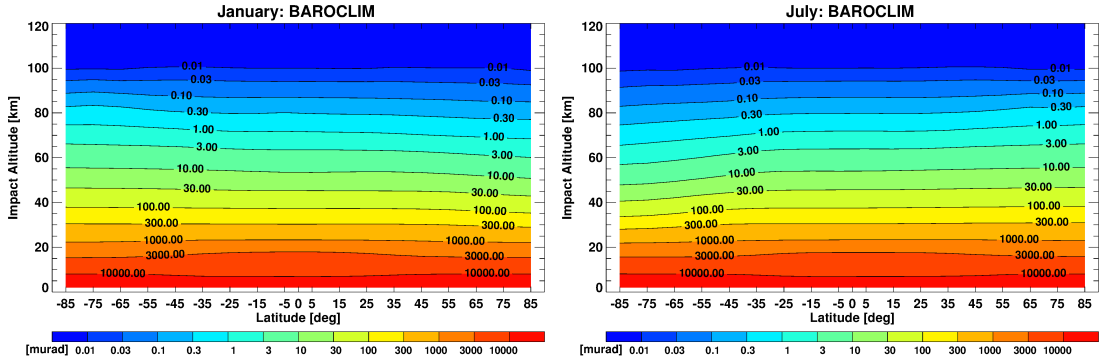


**Figure 4.1:** BAROCLIM model as a function of function of latitude and impact altitude for January (left) and July (right). BAROCLIM model is calculated with 18 zonal harmonics coefficients and 128 Chebychev coefficients.

isolines above and below. Fixing an annual mean bending angle (see Figure 1a in Ringer and Healy 2008), it usually reaches highest altitudes in the tropics and decreases in altitude with increasing latitude. The 0.01 rad isoline, however, increases with latitude: it reaches up to approximately 7 km at low latitudes and increases to 8 km at high latitudes.

## 4.2 Comparison of the BAROCLIM spectral model and MSIS

The BAROCLIM spectral model is validated using profiles from the MSIS climatology. For this purpose, I extract MSIS profiles at the mean tangent point location of F3C measurements, which entered into the calculation of mean RO bending angles (see Chapter 2). Since I use the MSIS model, which has a monthly temporal resolution and does not depend on solar activity nor on local apparent solar time, "co-location" just means spatial co-location but not close temporal co-location. In order to calculate monthly mean 10°-zonal mean MSIS fields, I average over these individual profiles.

Differences between the BAROCLIM spectral model and the mean MSIS fields are shown in Figure 4.2. In general, the differences are positive (i.e., BAROCLIM bending angles are larger than MSIS bending angles) below approximately 40 km with differences being smaller than 5 % everywhere apart from the tropical tropopause region. These larger differences in the tropical tropopause region might be attributed to the better representation of the sharp tropical tropopause in BAROCLIM. Larger negative differences (i.e., BAROCLIM < MSIS) up to 20 % are found from 40 km to 90 km. Above 90 km differences vary with latitude. Largest (positive) differences >20 % are found in the summer

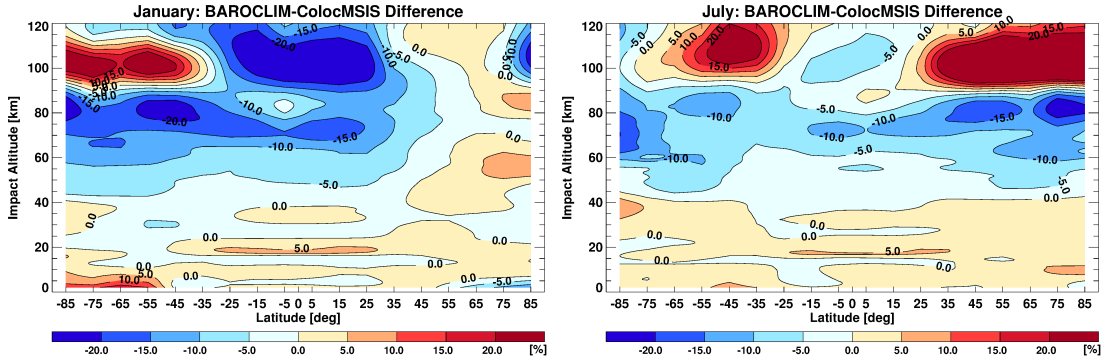


**Figure 4.2:** Systematic differences between the BAROCLIM spectral model and MSIS bending angles as a function of latitude and impact altitude for January and July.

hemisphere above 100 km.

Since BAROCLIM includes recent state-of-the-art measurements and systematic BAROCLIM errors (e.g., due to residual ionospheric errors, local multipath, or orbit determination) are believed to be distinctively smaller than these observed differences, BAROCLIM minus MSIS differences might be attributable to deficiencies of the MSIS climatological model.

## 4.3 Comparison of the BAROCLIM spectral model and ECMWF

Since December 2006 ECMWF operationally assimilates RO data below 50 km (Healy 2007), which means that ECMWF and RO data are not independent anymore. At high altitudes, however, ECMWF assumes very large RO observational errors, which limits the impact of RO on the quality of ECMWF analysis fields. Systematic differences between the BAROCLIM spectral model and mean ECMWF analysis profiles therefore provide valuable information about the quality of ECMWF analysis fields, especially at high altitudes.

The mean ECMWF field is obtained by averaging over all ECMWF profiles co-located to F3C measurements, which entered into the calculation of mean RO bending angles. In this case, "co-location" actually means spatial and temporal co-location because individual profiles are extracted from the ECMWF field closest to RO measurement time. Furthermore, the profile is extracted at mean RO event location. In order to calculate monthly mean 10°-zonal mean ECMWF fields, I again average over these individual profiles.

Figure 4.3 shows some interesting features. Due to the assimilation of RO data in ECMWF analyses, relative differences below approximately 35 km are, in general, small and rarely exceed 0.5 %. Below approximately 15 km, however, larger differences can be

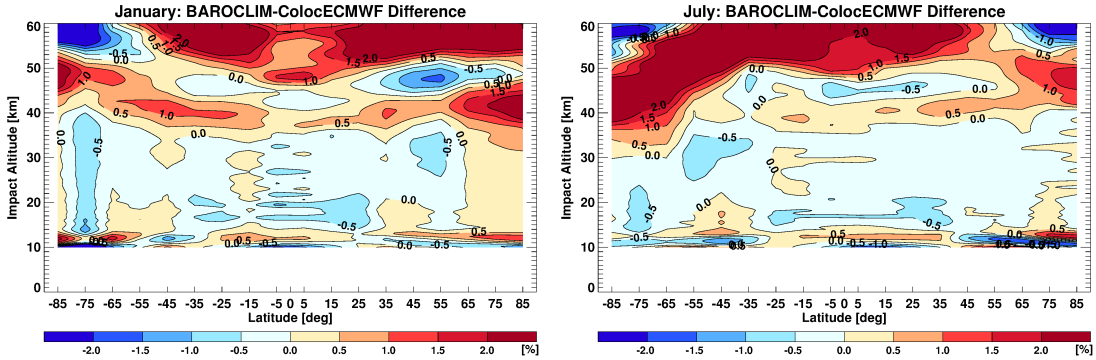


**Figure 4.3:** Systematic differences between the BAROCLIM spectral model and ECMWF bending angles as a function of latitude and impact altitude for January and July.

found, which might be attributable to the bending angle merge from mean RO bending angles to fitted MSIS profiles. Right above 35 km there is a "bent band" of positive BAROCLIM minus ECMWF differences with values reaching 1.0 %. Above 50 km differences are even larger than 2 %. These differences might be attributable to ECMWF rather than to BAROCLIM because differences of ECMWF to other satellite data, e.g., from the Michelson Interferometer for Passive Atmospheric Sounding (MIPAS) instrument onboard the European Environmental Satellite (ENVISAT) show similar results in temperature (not shown). Differences between 40 km and 50 km are known biases in ECMWF analyses (S. Healy, ECMWF, personal communication, 2012).

# 5 Summary, conclusions, and outlook

Figure 5.1 summarizes how the BAROCLIM spectral model was constructed. In a first study Foelsche and Scherllin-Pirscher (2012) calculated monthly mean RO bending angles. The generation of the BAROCLIM field and the BAROCLIM spectral model were performed in this study.

BAROCLIM input data were F3C closed-loop excess phase and orbit data provided by UCAR/CDAAC (version 2010.2640). These level 1 data from August 2006 to July 2011 were used to calculate individual ionosphere-corrected, non-optimized bending angle profiles utilizing the WEGC OPSv55 processing (revision 2871).

Quality control was applied to individual bending angle profiles checking data reliability and noise. Profiles, which passed quality control were used to calculate monthly mean bending angles (i.e., bending angles, which are typical for one month) for 10°-zonal bands. These mean bending angles were only available above 8 km because F3C closed-loop data do not reach below this level. Depending on atmospheric conditions and on data noise, mean bending angles are negative above 80 km to 90 km impact altitude, which is not physical for neutral atmospheric bending angles. However, the generation of a spectral model requires reliable knowledge of bending angles at the surface and at very high altitudes (theoretically at infinity) and for that reason I extended monthly mean bending angles with background information obtained from the MSIS climatology.

To get these MSIS profiles, I searched for the best-fitting MSIS profiles between 10 km and 15 km (lower transition) and between 60 km and 80 km (upper transition) on a $5° \times 10°$ latitude-longitude grid. These bottom and top best-fitting profiles were then multiplied with a fit factor, which was obtained from linear regression applied to the same impact altitude ranges (10 km to 15 km and 60 km to 80 km, respectively). Mean bending angles profiles and background profiles were combined by using a cosine transition from 10 km to 15 km and by applying statistical optimization from 60 km to 80 km. These monthly mean 10°-zonal mean bending angles, which reach from the surface to very high altitudes, are referred to the BAROCLIM field.

Finally, I expanded BAROCLIM bending angles into Chebychev polynomials and zonal harmonics. Smallest differences between the 10°-zonal mean BAROCLIM field and the BAROCLIM spectral model were found for 128 Chebychev coefficients and 18 zonal harmonics coefficients. This BAROCLIM spectral model even represents the sharp tropical tropopause but due to the merge of mean RO bending angles and MSIS below 15 km, the

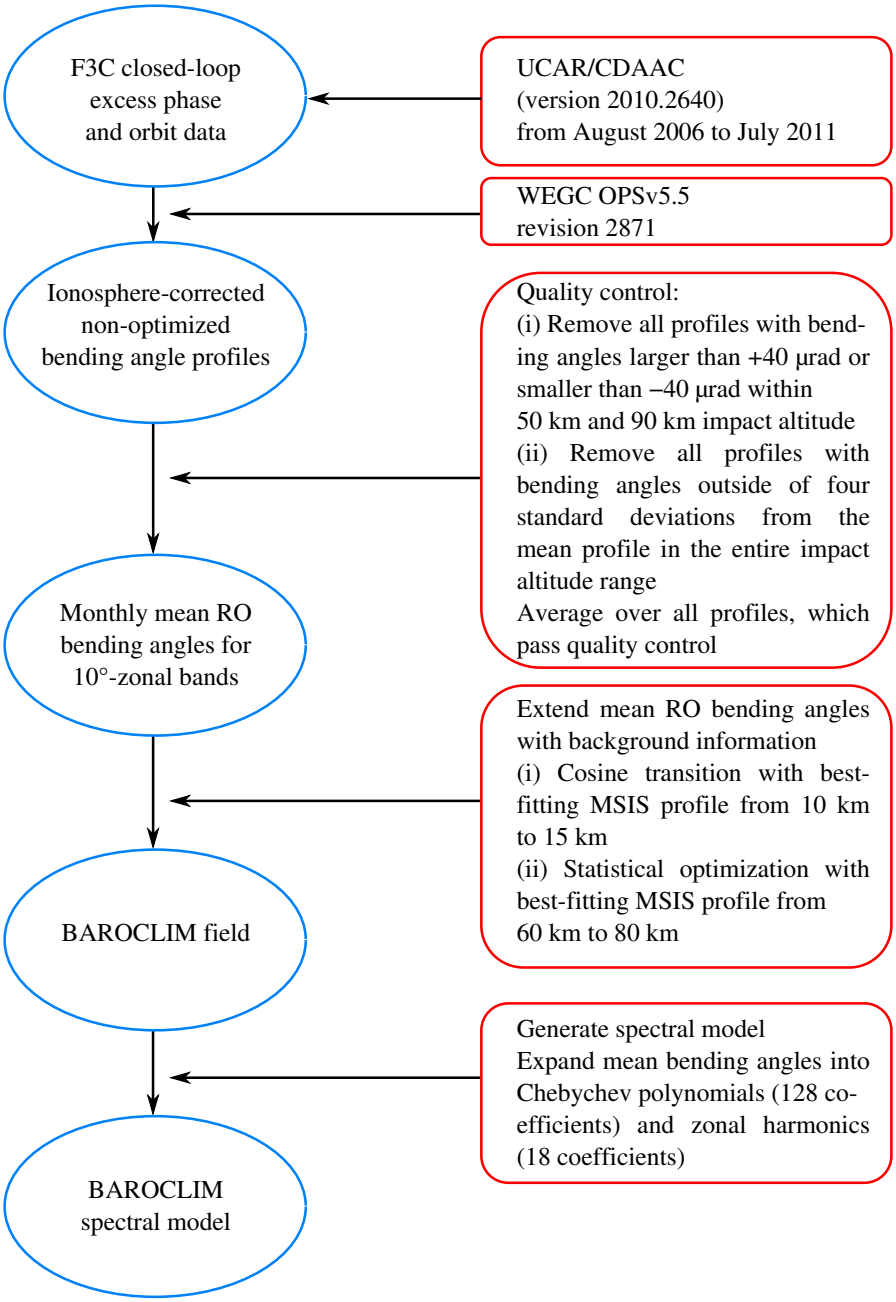


**Figure 5.1:** Flowchart summarizing of the BAROCLIM construction.

model should not be used in the lower and middle troposphere.

Differences between the BAROCLIM spectral model and MSIS are comparatively small (<10 % below 60 km). Above that height differences increase and get larger than 20 % above 80 km. Differences between the BAROCLIM spectral model and ECMWF are distinctively smaller but ECMWF operationally assimilates RO data since December 2006. Nevertheless, there are interesting features particularly above 35 km, e.g., a band of positive BAROCLIM minus ECMWF systematic differences with values reaching 1.0 % above 40 km. Above 50 km these differences are even larger than 2 %.

The BAROCLIM spectral model can be used for bending angle initialization in the RO retrieval. I already performed a very first test using BAROCLIM for statistical optimization. I used CHAllenging Mini-Satellite Payload (CHAMP) and F3C excess phase and orbit data from UCAR/CDAAC from January 15, 2008 and July 15, 2008 (to increase the number of CHAMP measurements, I used data for three consecutive days, i.e., January/July 14 to 16, 2008) and used the WEGC End-to-End Generic Occultation Performance Simulation and Processing System (EGOPS) (a slightly modified version of revision 3072) software to retrieve bending angle, refractivity, and dry atmospheric parameters.

For bending angle initialization, I used co-located profiles from BAROCLIM and MSIS as well as searched and fitted BAROCLIM and MSIS profiles. In this context, I use the search- and fit-algorithm described by Gobiet and Kirchengast (2004, enhanced IGAM high-altitude retrieval scheme). Figure 5.2 shows these results relative to ECMWF. For all statistical optimization methods, for both satellite missions, and both months, systematic differences in refractivity and dry temperature are close to zero below approximately 25 km to 30 km.

However, above 35 km in refractivity, and above 25 km to 30 km in dry temperature systematic differences and standard deviation relative to ECMWF strongly depend on the background used for bending angle initialization. If BAROCLIM is used as background, refractivity systematic differences are within ±2 % in the entire altitude range from 10 km to 60 km but if MSIS is used as background, refractivity systematic differences can be as large as 7 % at high altitudes (CHAMP data in July 2008).

Using BAROCLIM for bending angle initialization, dry temperature systematic differences are, in general, within ±3 K up to approximately 45 km. Above that height, differences increase to 10 K. Standard deviations are distinctively larger using the search- and fit-algorithm than using co-located profiles. This might be caused by the fit, which is good within the fit-range (i.e., from 35 km to 55 km altitude) but unrealistically shifts the profile outside of the fit-range.

While a detailed analysis of these results goes beyond the scope of this study, it clearly shows the potential of BAROCLIM to be used for bending angle initialization in RO retrieval algorithms.

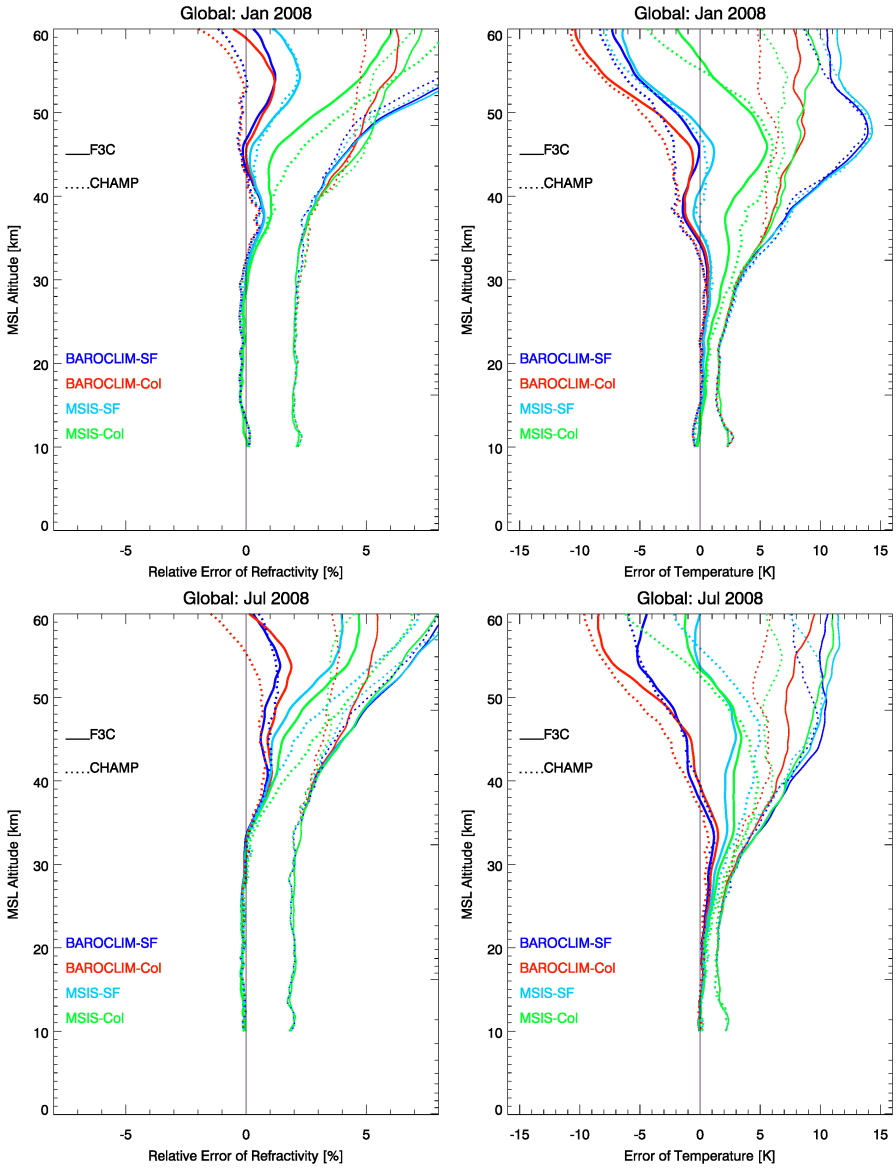


**Figure 5.2:** Systematic difference and standard deviation of CHAMP and F3C relative to ECMWF in January (top) and July (bottom) as a function of impact altitude up to 60 km. Results are shown for refractivity (left) and dry temperature (right). CHAMP and F3C bending angles (dotted and solid lines, respectively) are statistically optimized with co-located (Col) or searched and fitted (SF) profiles, either from BAROCLIM (blue and red) or from MSIS (light blue and green).

# Acknowledgments

I would like to thank Kent B. Lauritsen (DMI) for the invitation to perform this visiting scientist activity. Furthermore, I would like to thank Stig Syndergaard (DMI) for sharing his knowledge on the generation of spectral models and for his invaluable feedback and tireless support during the last few months. This study would not have been possible without his help. I also want to thank Gottfried Kirchengast and Marc Schwärz for scientific discussions. I am grateful to CDAAC/UCAR for providing F3C data, ECMWF for providing analysis data.

# List of Figures

# List of Tables

# References

Ao, C. O., A. J. Mannucci, and E. R. Kursinski (2012). "Improving GPS radio occultation stratospheric refractivity retrievals for climate benchmarking." *Geophys. Res. Lett.* 39, L12701. DOI: 10.1029/2012GL051720 (cit. on p. 7).

Danzer, J., B. Scherllin-Pirscher, and U. Foelsche (2013). "Systematic residual ionospheric errors in radio occultation data and a potential way to minimize them." *Atmos. Measur. Tech. Discuss.* 6, pp. 1979–2008. DOI: amt-2012-287 (cit. on p. 29).

Foelsche, U. and B. Scherllin-Pirscher (2012). *Development of bending angle climatology from RO data*. CDOP Visiting Scientist Report 14. Ref: SAF/GRAS/DMI/REP/VS14/001, July 2012. GRAS-SAF (cit. on pp. 6, 8, 9, 12, 15, 36).

Gleisner, H. and S. B. Healy (2013). "A simplified approach for generating GNSS radio occultation refractivity climatologies." *Atmospheric Measurement Techniques* 6, pp. 121–129. DOI: 10.5194/amt-6-121-2013 (cit. on p. 7).

Gobiet, A. and G. Kirchengast (2004). "Advancements of Global Navigation Satellite System radio occultation retrieval in the upper stratosphere for optimal climate monitoring utility." *J. Geophys. Res.* 109, D24110. DOI: 10.1029/2004JD005117 (cit. on p. 38).

Hajj, G. A., E. R. Kursinski, L. J. Romans, W. I. Bertiger, and S. S. Leroy (2002). "A technical description of atmospheric sounding by GPS occultation." *J. Atmos. Solar-Terr. Phys.* 64.4, pp. 451–469. DOI: 10.1016/S1364-6826(01)00114-6 (cit. on p. 7).

Healy, S. (2007). "Operational assimilation of GPS radio occultation measurements at ECMWF." *ECMWF Newsletter* 111, pp. 6–11 (cit. on p. 34).

Hedin, A. E. (1991). "Extension of the MSIS thermosphere model into the middle and lower atmosphere." *J. Geophys. Res.* 96, A2, pp. 1159–1172. DOI: doi:10.1029/90JA02125 (cit. on p. 10).

Ho, S.-P. et al. (2012). "Reproducibility of GPS radio occultation data for climate monitoring: Profile-to-profile inter-comparison of CHAMP climate records 2002 to 2008 from six data centers." *J. Geophys. Res.* 117, D18111. DOI: 10.1029/2012JD017665 (cit. on p. 7).

Høeg, P., A. Hauchecorne, G. Kirchengast, S. Syndergaard, B. Belloul, R. Leitinger, and W. Rothleitner (1995). *Derivation of atmospheric properties using a radio occultation technique*. DMI Sci Rep 95-4. Danish Meteorological Institute, Copenhagen, Denmark, p. 208 (cit. on p. 10).

Kursinski, E. R., G. A. Hajj, J. T. Schofield, R. P. Linfield, and K. R. Hardy (1997). "Observing Earth's atmosphere with radio occultation measurements using the Global Positioning System." *J. Geophys. Res.* 102, D19, pp. 23429–23465 (cit. on pp. 7, 32).

Melbourne, W. G., E. S. Davis, C. B. Duncan, G. A. Hajj, K. R. Hardy, E. R. Kursinski, T. K. Meehan, L. E. Young, and T. P. Yunck (1994). "The application of spaceborne GPS to atmospheric limb sounding and global change monitoring." *JPL Publication* 94–18, p. 147 (cit. on p. 7).

Press, W. H., B. P. Flannery, S. A. Teukolsky, and W. T. Vetterling (1986). *Numerical Recipes: The Art of Scientific Computing*. New York, NY, USA: Cambridge University Press (cit. on pp. 16–18, 22–24).

Rieder, M. J. and G. Kirchengast (2001). "Error analysis and characterization of atmospheric profiles retrieved from GNSS occultation data." *J. Geophys. Res.* 106, D23, pp. 31755–31770 (cit. on p. 13).

Ringer, M. A. and S. B. Healy (2008). "Monitoring twenty-first century climate using GPS radio occultation bending angles." *Geophys. Res. Lett.* 35, L05708. DOI: 10.1029/2007GL032462 (cit. on pp. 32, 33).

Smith, E. and S. Weintraub (1953). "The constants in the equation for atmospheric refractive index at radio frequencies." *Proc. IRE* 41, pp. 1035–1037 (cit. on p. 32).

Spiegel, M. R., ed. (1979). *Handbuch für Mathematik: Formeln und Tabellen, Theorie und Anwendung*. Schaum's Outline. Düsseldorf, New York, St. Louis: McGraw-Hill, p. 271 (cit. on p. 22).

Steiner, A. K. et al. (2013). "Quantification of structural uncertainty in climate data records from GPS radio occultation." *Atmos. Chem. Phys.* 13, pp. 1469–1484. DOI: 10.5194/acp-13-1469-2013 (cit. on p. 7).

# List of Acronyms

## B

**BAROCLIM** Bending Angle Radio Occultation Climatology. 6–11, 14, 16–20, 22, 23, 26–28, 30–33, 35, 37, 43, 45, 47, 49

## C

**CDAAC** COSMIC Data Analysis and Archive Center. 9, 35, 37, 39

**CDOP** Continuous Development and Operations Phase. 7

**CHAMP** CHAllenging Mini-Satellite Payload. 37

**CoI** co-located. 37

**COSMIC** Constellation Observing System for Meteorology, Ionosphere, and Climate. 6, 7, 9

## D

**DMI** Danish Meteorological Institute. 7, 9, 17, 39

## E

**ECMWF** European Centre for Medium-Range Weather Forecasts. 6–8, 10, 33, 35, 37, 39, 49

**EGOPS** End-to-End Generic Occultation Performance Simulation and Processing System. 37

**ENVISAT** Environmental Satellite. 33

## F

**F3C** FORMOSAT-3/COSMIC. 6, 7, 9, 14, 32, 33, 35, 37, 39

**FORMOSAT-3** FORMOsa SATellite mission-3. 6, 7

## G

**GFZ** German Research Centre for Geosciences. 7

**GNSS** Global Navigation Satellite System. 7

**GPS** Global Positioning System. 7

## J

**JPL** Jet Propulsion Laboratory. 7

## L

**LEO** Low Earth Orbit. 7

**LT** Local Time. 9

## M

**MIPAS** Michelson Interferometer for Passive Atmospheric Sounding. 33

**MSIS** Mass Spectrometer and Incoherent Scatter Radar. 6–18, 28, 30, 32, 33, 35, 37, 47

## N

**NCAR** National Center for Atmospheric Research. 7

## O

**OPSv55** Occultation Processing System Version 5.5. 9, 35

## R

**RAER** Retrieval to A priori Error Ratio. 13

**RO** Radio Occultation. 6–16, 30, 32, 33, 35, 37

**ROM** Radio Occultation Meteorology. 7

## S

**SAF** Satellite Application Facility. 7

**SF** searched and fitted. 37

## U

**UCAR** University Corporation for Atmospheric Research. 7, 9, 35, 37, 39

**UTLS** Upper Troposphere–Lower Stratosphere. 6

## W

**WEGC** Wegener Center for Climate and Global Change. 7, 9, 35, 37

## Z

**zRAER50** impact altitude, where the retrieval to a priori error ratio equals 50 %. 13

# A The BAROCLIM spectral model for all months

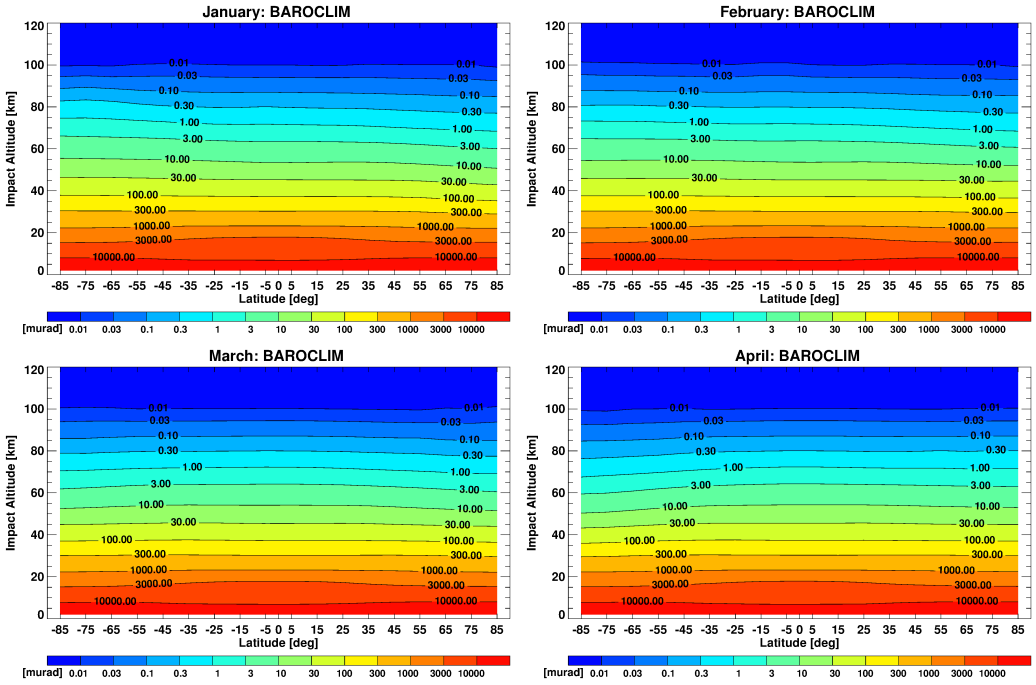


**Figure A.1:** BAROCLIM model as a function of function of latitude and impact altitude for January to April. BAROCLIM model is calculated with 18 zonal harmonics coefficients and 128 Chebychev coefficients.

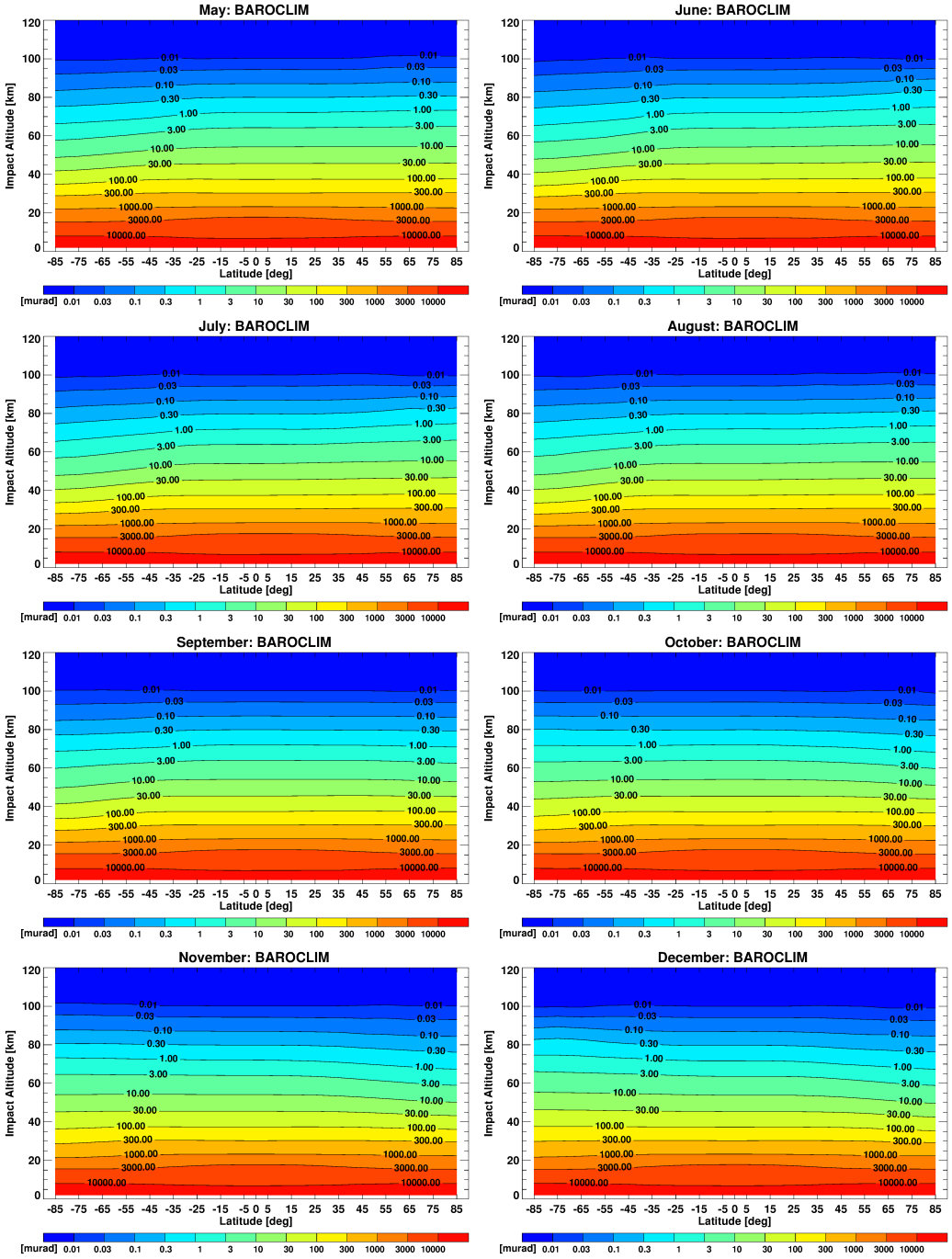


**Figure A.2:** BAROCLIM model as a function of function of latitude and impact altitude for May to December. BAROCLIM model is calculated with 18 zonal harmonics coefficients and 128 Chebychev coefficients.

# B BAROCLIM field minus BAROCLIM spectral model differences for all months

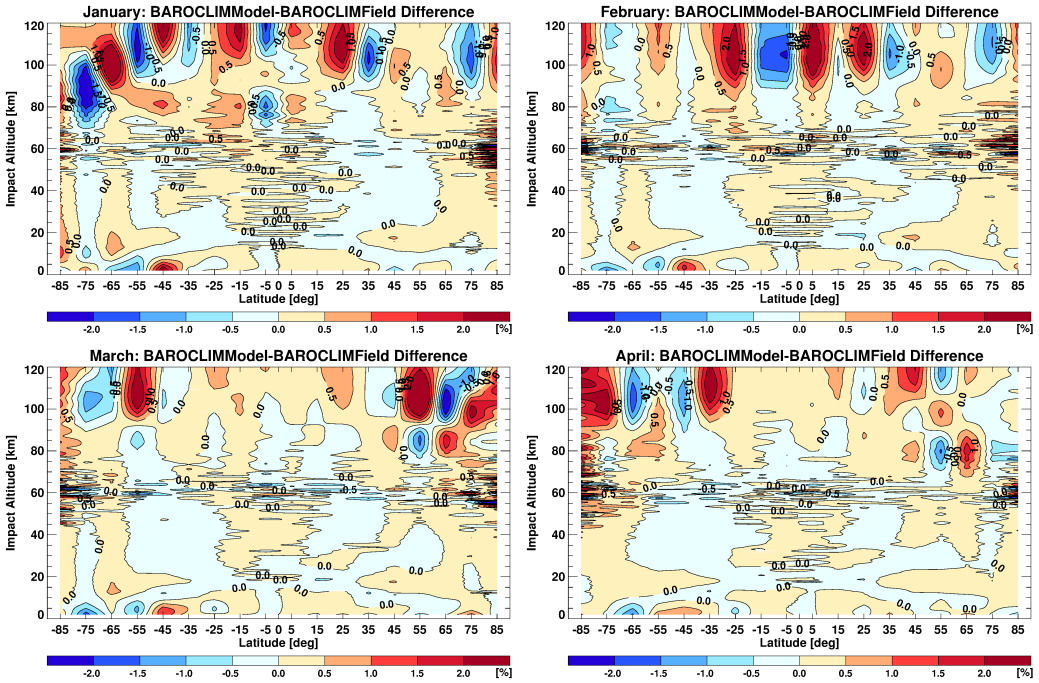


**Figure B.1:** Systematic difference between the BAROCLIM field and the BAROCLIM spectral model (in %) as a function of latitude and impact altitude for January to April. The BAROCLIM spectral model is calculated with 18 zonal harmonics and 128 Chebychev coefficients.

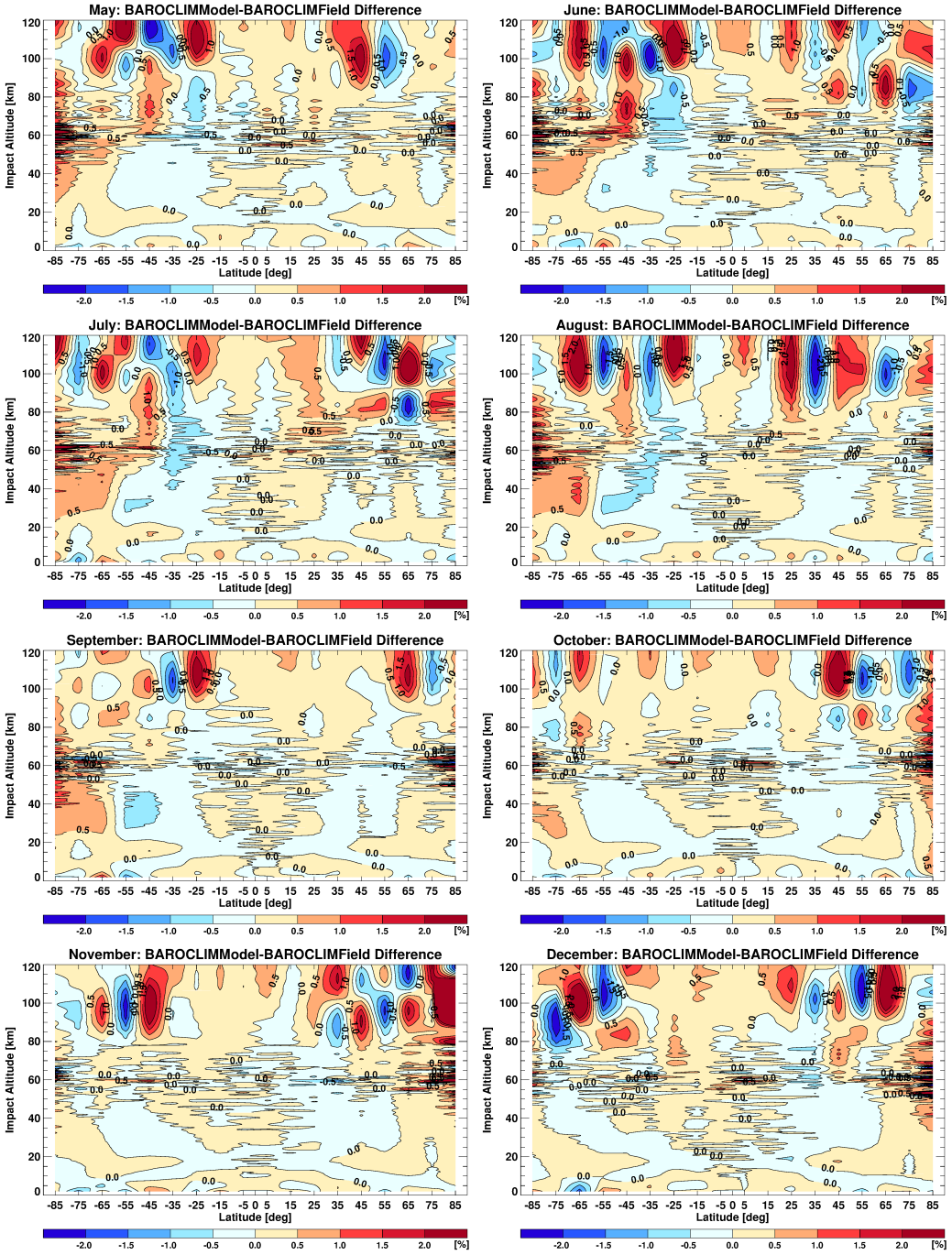


**Figure B.2:** Systematic difference between the BAROCLIM field and the BAROCLIM spectral model (in %) as a function of latitude and impact altitude for May to December. The BAROCLIM spectral model is calculated with 18 zonal harmonics and 128 Chebychev coefficients.

# C BAROCLIM minus MSIS differences for all months

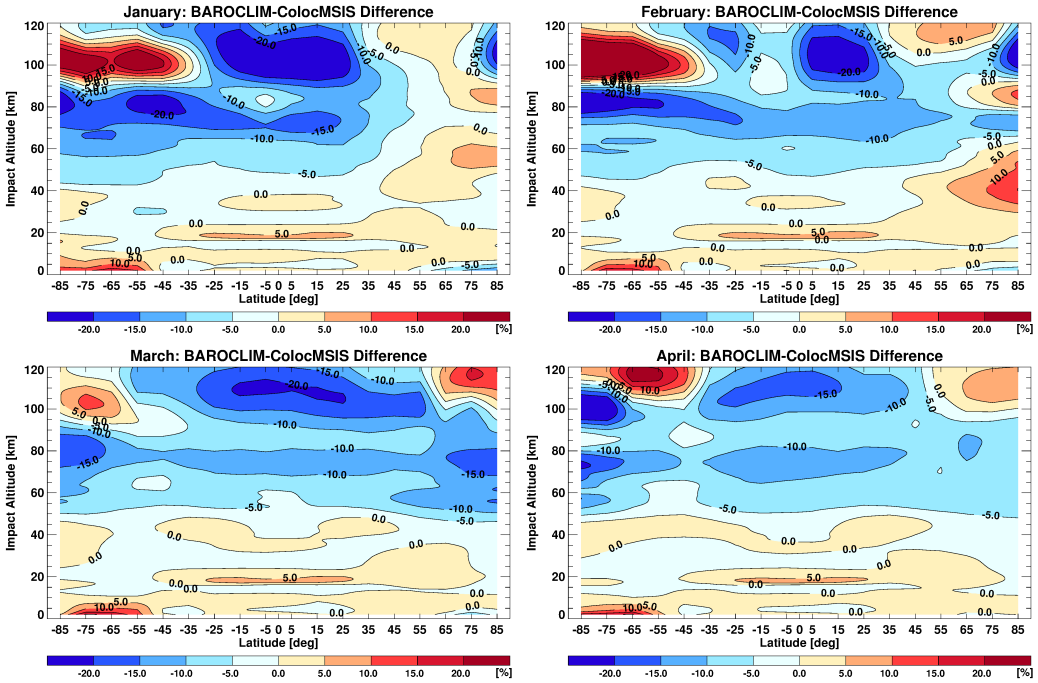


**Figure C.1:** Systematic differences between the BAROCLIM spectral model and MSIS bending angles as a function of latitude and impact altitude for January to April.

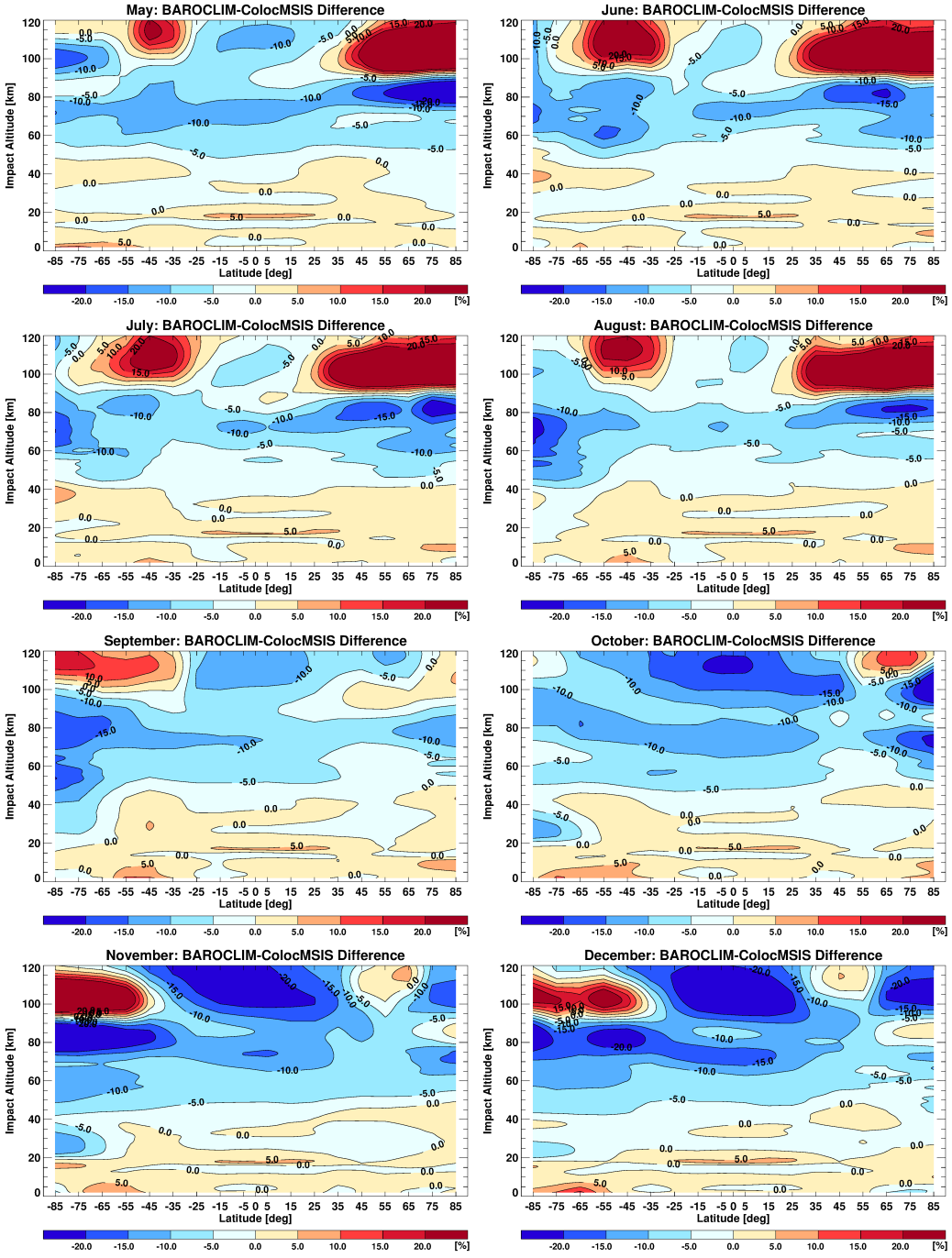


**Figure C.2:** Systematic differences between the BAROCLIM spectral model and MSIS bending angles as a function of latitude and impact altitude for May to December.

# D BAROCLIM minus ECMWF differences for all months

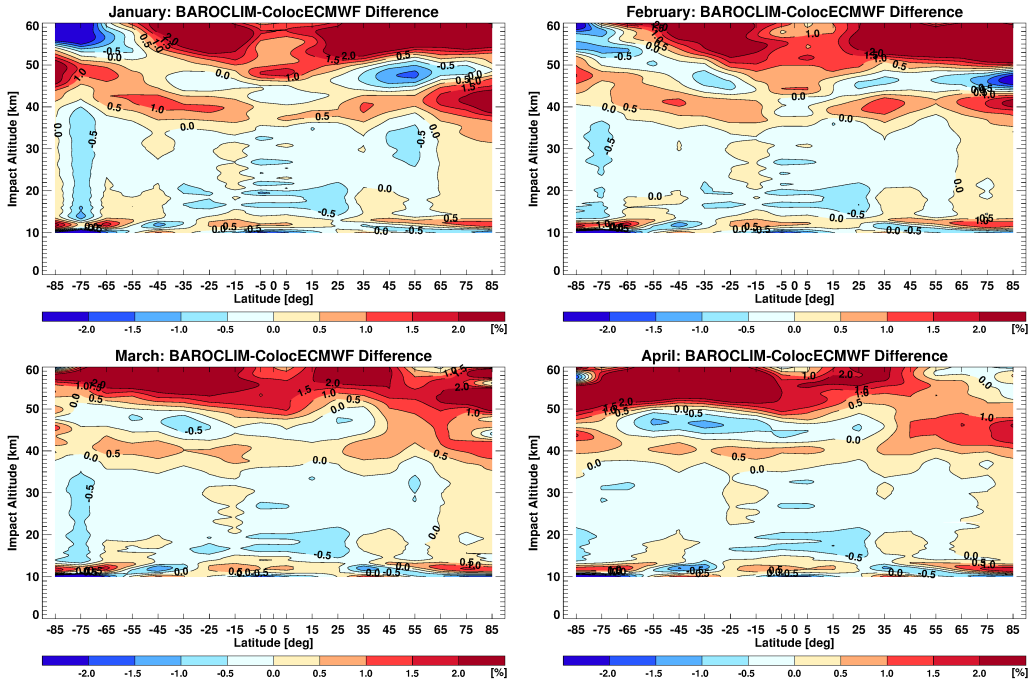


**Figure D.1:** Systematic differences between the BAROCLIM spectral model and ECMWF bending angles as a function of latitude and impact altitude for January to April.

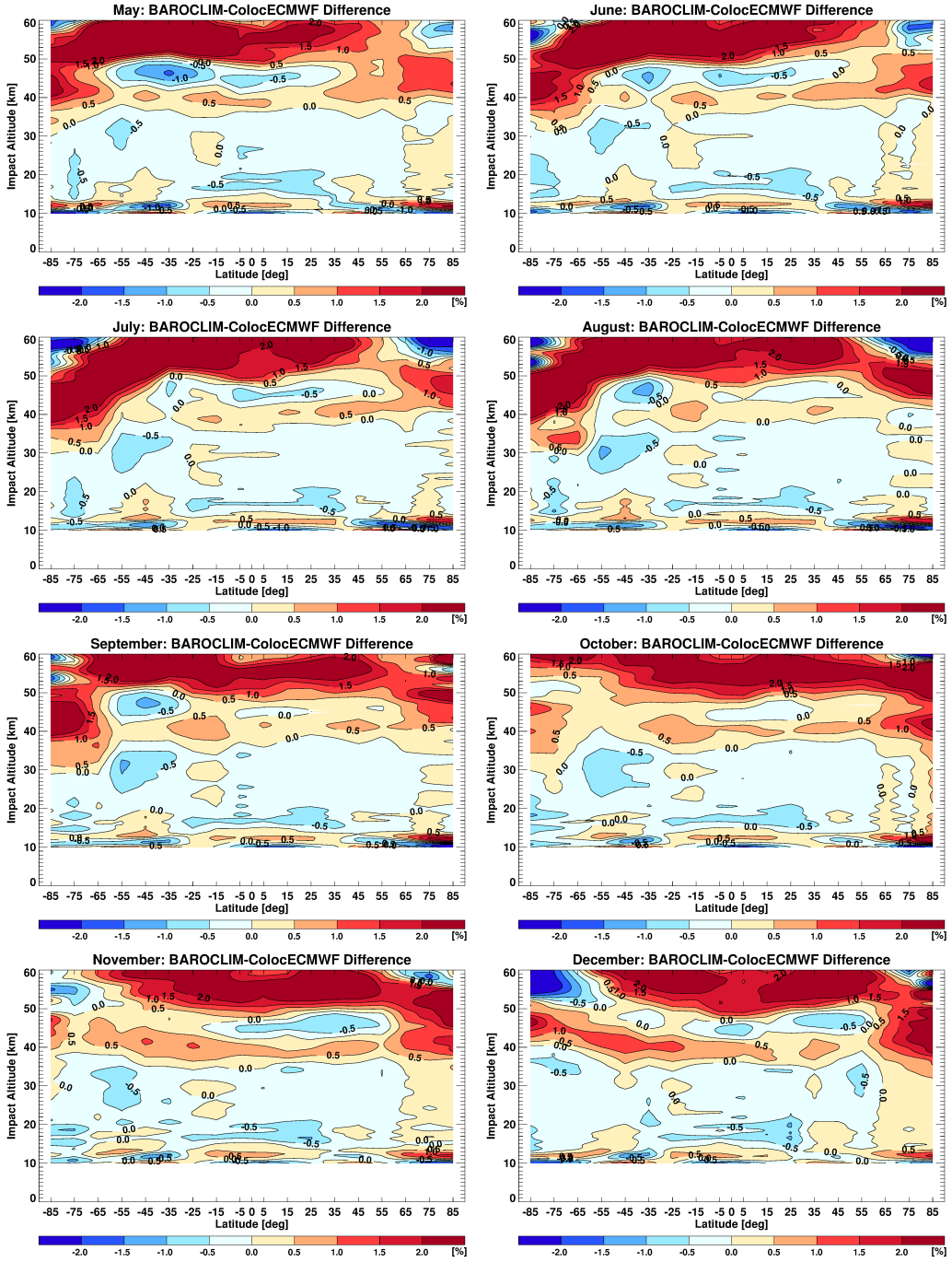


**Figure D.2:** Systematic differences between the BAROCLIM spectral model and ECMWF bending angles as a function of latitude and impact altitude for May to December.